Generation of hiPSC-derived brain microvascular endothelial cells using a combination of directed differentiation and transcriptional reprogramming strategies

Ronak Patel[1,*], Aomeng Cui[2,*], Patrick Bosco[1,*], Ugur Akcan[2], Emily Richters[1], Paula Barrilero Delgado[3] Dritan Agalliu[2,4,#] and Andrew A. Sproul[1,4,#]

[1]Taub Institute for Research on Alzheimer's Disease and the Aging Brain, Columbia University Irving Medical Center, New York, NY, USA

[2]Department of Neurology, Columbia University Irving Medical Center, New York, NY, USA

[3]Francisco de Vitoria University, Madrid, Spain

[4]Department of Pathology and Cell Biology, Columbia University Irving Medical Center New York, New York, NY, USA

[*]Equal first authors

#Corresponding authors:

Andrew Sproul Ph.D. Email – aas2003@cumc.columbia.edu

Dritan Agalliu Ph.D. Email – da191@cumc.columbia.edu

Lead contact:

Andrew Sproul Ph.D. Email – aas2003@cumc.columbia.edu

Keywords:

blood-brain barrier, NVU, iPSCs, directed differentiation, transcriptional reprogramming, FOXF2, ZIC3, oligomeric Aβ

SUMMARY

The blood-brain barrier (BBB), formed by specialized brain microvascular endothelial cells (BMECs), regulates brain function in health and disease. *In vitro* modeling of the human BBB is limited by the lack of robust protocols to generate BMECs from human iPSCs (hiPSCs). Here, we report generation of reprogrammed BMECs (rBMECs) through combining hiPSC differentiation into BBB-primed endothelial cells (bpECs) and reprogramming with two BBB transcription factors, FOXF2 and ZIC3. rBMECs express a subset of the BBB gene repertoire including tight junctions and transporters, exhibit higher paracellular barrier properties, lower caveolar-mediated transcytosis, and equivalent p-glycoprotein activity compared to primary HBMECs, and can be activated by oligomeric Aβ42. We then generated an hiPSC-derived 3D neurovascular system that incorporates rBMECs, pericytes, and astrocytes using the MIMETAS platform. This novel 3D system closely resembles the *in vivo* BBB at structural and functional levels and can be used to study pathogenic mechanisms of neurological diseases.

INTRODUCTION

Brain microvascular endothelial cells (BMECs) possess highly specialized structural and functional properties that form the blood-brain barrier (BBB). Interactions with pericytes and astrocytes via the vascular basement membrane are critical to induce and maintain these unique BMEC properties, which include: (1) tight junctions which restrict paracellular flux, (2) reduced transcytosis due to the presence of few caveolae, (3) specific transporters that regulate the passage of nutrients and restrict harmful pathogens, and (4) low expression of leukocyte adhesion molecules (LAMs)[1-5]. In many neurological diseases, such as multiple sclerosis (MS) or stroke, BMEC dysfunction exacerbates BBB permeability leading to more severe neuroinflammation and neuronal damage[2,6,7]. For neurodegenerative diseases like Alzheimer's disease (AD) and Huntington's disease (HD), the accumulation of damaging protein aggregates of amyloid-β or mutant huntingtin in patient postmortem brain capillaries, respectively, suggests that BBB disruption contributes to disease progression and cognitive decline[8-14].

Rodent models, although useful for studying mechanisms of central nervous system (CNS) diseases, differ from humans at the cellular level and fail to capture patient heterogeneity in multifactorial conditions[15,16]. Recent studies have shown that non-neuronal gene expression differs most strikingly between mouse and human cortices[16]. In traumatic brain injury (TBI), the mitigating role of patient comorbidities is not captured in rodents, which have homogenous injuries and responses; in AD, rodent models do not recapitulate the genetic diversity of patients[17-19]. Accordingly, clinical trials for both TBI and AD featuring therapies effective in rodents have largely failed[16]. Therefore, there is

significant interest in developing *in vitro* human BMEC (HBMEC) systems to model human neurological diseases and develop drugs that can penetrate the brain[20-23]. Primary HBMECs are scarce, heterogenous, and dedifferentiate in culture[24-26]. Human induced pluripotent stem cells (hiPSCs) are a promising alternative due to their reproducibility, scalability, and ability to model healthy and pathological states, including via isogenic models generated by CRISPR-mediated genome editing. Over the past decade, several protocols have been developed claiming to generate a homogenous population of endothelial cells with high transendothelial electrical resistance (TEER) and expression of tight junction proteins, termed iPSC-derived BMECs (iBMECs)[27-33]. However, we recently demonstrated that iBMECs are transcriptomically and functionally analogous to epithelial cells, or at minimum have a mixed epithelial identity[34]. Moreover, these iBMECs fail to respond to inflammatory stimuli, which limits their ability to model human neurological diseases[35]. Recently, novel methods used extended passaging of endothelial progenitor cells (EPCs) to generate ECs (EPC-ECs), which had suitable barrier properties but limited response to inflammatory stimuli[35-38]. Understanding molecular mechanisms of the BBB in healthy and pathological states thus depends upon the ability to generate bona fide human brain ECs.

Activation of Wnt-β-catenin signaling is necessary for the establishment and maturation of the BBB[39-41]. Previous methods have mimicked the environmental cues of Wnt exposure to promote differentiation of iPSC-derived ECs into BBB-forming cells[28,29,38]. While these approaches improved certain BBB features, such as upregulation of facilitated glucose transporter member 1 (GLUT-1), activation of Wnt signaling is not sufficient to drive endothelial identity in iBMECs[28] or induce expression of efflux transporters in naïve EPC-ECs[33]. Recently, transcriptome and chromatin accessibility comparisons of endothelial cells from various organs have identified several transcription factors (TFs) including FOXF2, FOXQ1, LEF1, and ZIC3 as being essential for BMEC identity [42,43]. FOXF2 has been observed in both endothelial cells [42,43] and pericytes [44], and is known to be involved in maintaining barrier integrity and low transcytosis[44]. ZIC3 is upregulated in development, suggesting an importance in establishment of the BBB[45]. Moreover, overexpression of FOXF2 and ZIC3 in primary human umbilical vein endothelial cells (HUVECs) was sufficient to upregulate BBB-specific gene expression[42], suggesting that these TFs could reprogram generic ECs into a BMEC identity with transcriptional and functional BBB features.

Here, we describe a novel protocol to generate iPSC-derived reprogrammed BMECs (rBMECs). This protocol combines an iPSC differentiation step into BBB-primed endothelial cells (bpECs)[46] with transcriptional reprogramming with two key BBB TFs: FOXF2 and ZIC3. rBMECs express increased levels of key BBB genes compared to primary HBMECs and bpECs, have physiologically high TEER,

exhibit lower transcytosis and equivalent efflux transport compared to HBMECs, and respond to angiogenic stimuli. In response to oligomerized amyloid-β (oAβ42) treatment, rBMECs respond robustly to upregulate intracellular adhesion molecule 1 (*ICAM1*), vascular cell adhesion molecule 1 (*VCAM1*), and E-selectin (*SELE*), all pro-inflammatory LAMs. Finally, rBMECs cocultured in a 3D microfluidic system with iPSC-derived astrocytes and pericytes demonstrate high levels of TEER and low paracellular and transcellular barrier permeability to tracers, closely resembling *in vivo* BBB states. Taken together, our rBMECs enable faithful *in vitro* modeling of the human BBB for future studies into disease pathogenesis and clinical therapies.

RESULTS

Reprogramming iPSC-derived bpECs into rBMECs

During development, the mesodermal layer of the mammalian embryo gives rise to the CNS vasculature, under the guidance of VEGF and Wnt-β-catenin signaling[47]. To mimic this approach, we differentiated iPSCs grown under feeder conditions into a mesodermal intermediate using BMP4, VEGF, and Thymosin β4 to generate BBB-primed ECs (bpECs) following a published protocol with some modifications[48]. We hypothesized that subsequent transduction of these bpECs with lentiviruses expressing BBB-critical TFs would generate brain-specific ECs. Thus, iPSC-derived rBMECs were generated via a two-stage approach (**Fig. 1A, Fig. S1A**). During the first stage, iPSCs were differentiated into bpECs via a mesodermal intermediate[48], purified by FACS on day 10 of differentiation for $CD31^+$/VE-$cadherin^+$ (Sort A), and expanded on collagen IV/fibronectin-coated dishes in human endothelial serum-free media supplemented with 1% human plasma-derived platelet poor serum, VEGF-A, bFGF and SB431542 (**Fig. 1B**). In the second stage, bpECs were reprogrammed into rBMECs via lentiviral overexpression of FOXF2 and ZIC3. bpECs transduced with FOXF2 and ZIC3 lentiviral particles were grown for 14 days and re-purified by FACS (Sort B) for expansion (**Fig. 1B**). By Sort B, bpECs without transduction expressed CD31 and VE-cadherin at a lower efficiency compared to rBMECs (**Fig. 1C**). Sort A efficiency for lines varied from 1.3-5.1% for IMR90 (cl.4), 3.9-7.4% for FA0000010 (FA10), and 2.4-3.3% for NCRM5 **(Fig. S1C)**; while Sort B efficiency ranged from 56.6-96.1% for IMR90, 83.7-92.3% for FA10, and 34.9-42.6% for NCRM5 (**Fig. S1D**). These double-sorted cells were reliably expanded as rBMECs for five passages after the re-purification step.

rBMECs express key markers and respond to an angiogenic stimulus

The majority of both bpECs and rBMECs expressed VE-cadherin, platelet/endothelial cell adhesion molecule (PECAM1/CD31), Zonula occludens-1 (ZO-1), Claudin-5, and Occludin by

immunofluorescence (IF) staining (**Fig. 1D-F, Fig. S1E-G**). However, rBMECs expressed elevated levels of tight junction markers Claudin-5 (8.1 fold) and Occludin (1.5 fold) compared to bpECs as assessed by western blot (**Fig. 1G-H**). Furthermore, rBMECs failed to stain positive for epithelial cellular adhesion molecule (EPCAM) as assessed by flow cytometry (**Fig. S1B)**, which suggests they are not epithelial in nature. Next, we stained endothelial cells for DAPI and Ki67 to calculate their proliferative index. When cultured without addition of growth factors (VEGF and bFGF), rBMECs proliferated at a similar rate to bpECs, which was lower than that of primary HBMECs **(Fig. 1I)**. To assess the ability of rBMECs to respond to an angiogenic stimulus, we scratched confluent endothelial monolayers, treated with basal media or media supplemented with an angiogenic cocktail consisting of human VEGF, bFGF, and hepatocyte growth factor (HGF), and observed cell migration **(Fig. S1H-I)**. By 36 hrs, rBMEC migration increased in response to the angiogenic cocktail (**Fig. 1J**). To compare the overall effect of the angiogenic cocktail treatment between cell types, we calculated an angiogenic potential. Both primary HBMECs and rBMECs exhibited comparable angiogenic potential, while bpECs responded more strongly to the angiogenic stimulus (**Fig. 1K)**.

Transcriptional profiling of rBMECs

To better characterize the molecular identity of rBMECs, we used bulk-RNAseq to examine BBB-related gene expression. We first generated principal component analysis (PCA) plots to evaluate the global rBMEC transcriptome. Compared to cell types from published datasets[34,49-51], rBMECs clustered most closely with endothelial cells and furthest apart from choroid plexus cells, epithelial cells, and iBMECs[34] (**Fig. 2A**). Together with our IF staining and flow cytometry data, this conclusively establishes that rBMECs have an endothelial identity. From the PCA analysis of only endothelial cell populations, rBMECs cluster closer to HBMECs and away from other peripheral ECs **(Fig. 2B).** To compare the rBMEC transcriptome to that of primary HBMECs, we evaluated our rBMECs for pivotal BBB genes such as tight junctions (TJs), transporters, receptor-mediated transcytosis, ECM components, and CNS EC identity genes (**Fig. 2C-F**). Tight junction markers *CLDN5*, *OCLN*, and *JAM2* along with transporters *SLC2A1*, *ABCC4,* and *SLC1A1* were also elevated in rBMECs compared to HBMECs (**Fig. 2C, 2D)**. rBMECs expressed higher levels of BBB identity markers *FOXF2*, *FOXQ1*, *ITM2A*, *PROM1*, *LRP8,* and *APCDD1* compared to primary HBMECs (**Fig. 2F**). ECM markers *COL4A1*, *COL4A2*, *LRP10* were similarly upregulated (**Fig. 2E**). Although rBMECs shared a more similar gene expression profile compared to bpECs **(Fig. 2B)**, we found upregulation of key BBB genes *ITIM2A*, *OCLN*, *CLDN5*, *TJP2*, *SLC2A1* and *COL4A1* **(Fig. S2A-F)**, suggesting improvement in BMEC properties. Furthermore, when we performed gene ontology (GO) analysis of the differentially expressed genes

(DEGs) upregulated in rBMECs compared to HBMECs, we found that pathways related to blood vessel development and blood-brain barrier maintenance were upregulated **(Fig. 2H)**. Moreover, rBMECs show reduced expression of leukocyte-adhesion molecule *VCAM1* and *SELP* compared to HBMECs (**Fig. 2E)** and bpECs (**Fig. S2C**), suggesting that rBMECs are in a resting, non-inflammatory state more indicative of CNS than peripheral vasculature. In summary, the rBMEC transcriptome has stronger expression of genes important for key BBB properties and identity compared to both primary HBMECs and bpECs.

Functional characterization of rBMECs

We next investigated the functional properties of rBMECs through a series of assays. To probe the barrier properties of rBMECs, we measured TEER with the ECIS instrument. rBMECs differentiated from the IMR90 line exhibited higher average TEER ($40.5 \pm 4.2\ \Omega*cm^2$) compared to bpECs ($25.0 \pm 0.4\ \Omega*cm^2$) or primary HBMECs ($24.7 \pm 3.0\ \Omega*cm^2$) in over 300 hours of recording and nearly two-fold increase in the area under the curve (AUC) for the last 100 hours compared to HBMECs (**Fig. 3A-B**). A similar elevation of TEER in rBMECs was observed in hiPSC lines FA10 and NCRM5 compared to HBMECs (**Fig. S3A-B, D-E**). Overall, our data indicate rBMECs show improved paracellular barrier properties compared to primary HBMECs. Next, we assessed rBMECs for caveolae-mediated transcytosis by incubating them with a fluorescently tagged bovine serum albumin (BSA) and using flow cytometry to assess for fold change in median fluorescence intensity (MFI) (**Fig. 3C-D**). rBMECs and bpECs had a lower level of BSA fluorescence compared to HBMECs (**Fig. 3D**), suggesting that caveolae-mediated transcytosis was decreased. Next, we assessed the function of p-glycoprotein transporter (PGP), which is known to efflux drugs from the brain to the blood[52]. The fluorescent probe rhodamine 123, which is effluxed by PGP,[53] was incubated with monolayer cultures of HBMECs, bpECs, and rBMECs for an hour, with and without prior treatment with a PGP-specific inhibitor PSC-833. Cells were subsequently analyzed for fold change in MFI by flow cytometry (**Fig 3E-G**). We subsequently calculated an efflux rate based on the change in MFI in the presence of inhibitor versus without inhibitor. HBMECs, bpECs, and rBMECs had comparable efflux rates in response to PSC-833, suggesting they have similar levels of PGP activity **(Fig. 3F**). rBMECs but not bpECs had a lower fold change in MFI compared to HBMECs **(Fig. 3G**) suggesting that more rhodamine 123 was effluxed overall. Taken together, this suggests that rBMECs have a stronger paracellular barrier and increased efflux of rhodamine compared to bpECs, although PGP-activity and caveolae-mediated transcytosis are similar. Compared to HBMECs, rBMECs have a superior paracellular barrier and decreased caveolae-mediated transcytosis.

We then investigated the ability of rBMECs to respond to a pro-inflammatory and disease-relevant stimulus: oligomeric amyloid-β (1-42) peptides (oAβ42). Most AD patients have amyloid deposits along their cerebral vasculature revealed in post-mortem brains studies[54-56]. Additional cerebrovascular pathologies found in AD brains include decreased microvascular density, vBM thickening, BMEC and pericyte damage, inflammatory changes in vessels, and microglial activation around blood vessels[40,57]. We first assessed if oAβ42 affected the paracellular barrier of rBMECs by TEER. rBMECs were challenged with 1 uM of oAβ42, and surprisingly, there was no change in TEER over 72 hours (**Fig. 3H-I**). We then extracted RNA and analyzed if oAβ42 induced endothelial activation via increased expression of adhesion molecules and chemokines. *VCAM-1* was increased by 5.2-fold, and *ICAM-1* was increased by 1.7 fold (**Fig. S3C**). Chemokine ligand 2 (*CCL2*), a major effector of ischemic stroke[58] and other BBB-compromising pathologies[59,60] and a powerful monocyte and T-cell attractant[58], was upregulated in rBMECs treated with oAβ42 (**Fig. S3C**). We then assessed the effects of a BBB-disrupting inflammatory cocktail comprised of TNFα and IL1β on rBMECs[61], which led to an immediate reduction in TEER over 24 hours **(Fig. S3F-G),** revealing that the barrier was disrupted by these inflammatory cytokines—unlike in our oAβ42 treated condition. To see more immediate effects of oAβ42, we treated rBMECs with 500 nM oAβ42 for 6 hours and analyzed by qPCR, western blot, and flow cytometry. We analyzed production of pro-inflammatory cytokines as possible effectors of oAβ42-mediated dysfunction. oAβ42 significantly increased mRNA expression of *IL-1β*, *IL-6*, and *TNFα* (**Fig. 3J**). Additionally, treatment of rBMECs with oAβ42 for 6 hours increased expression of ICAM-1 and VCAM-1 at the transcript and surface protein levels as measured by qPCR and flow cytometry respectively (**Fig. 3K-M)**. *CCL2* and *E-SELECTIN* mRNA levels were also significantly upregulated **(Fig. 3K)**, suggesting that oAβ42 primes the brain vasculature to interact with circulating immune cells. These data are consistent with recent findings that treating primary HBMECs with conditioned media from hiPSC-derived cortical neurons harboring the $APP^{Swe/Swe}$ mutation (KM670/671NL) significantly upregulates *VCAM-1*, *ICAM-1*, *E-SELECTIN*, and *CCL2*[62]. Finally, we sought to identify potential signaling pathways that might contribute to oAβ42-induced activated endothelial phenotypes in rBMECs. We found that signal transducer and activator of transcription 3 (STAT3), a key mediator of proinflammatory processes in brain endothelial cells[63,64], had elevated phosphorylation in rBMECs treated with oAβ42 **(Fig. S3H-I).** Together, these data indicate that β-amyloid peptides act as a pro-inflammatory stimulus to upregulate a subset of endothelial activation genes and may contribute to increased interactions at the immune-BBB interface but does not disrupt the paracellular barrier. In summary, rBMECs have strong functional properties and are a suitable model to study potential impact of disease-relevant stimuli and immune cell interactions at the BBB.

Modeling 3D NVUs using rBMECs and hiPSC-derived astrocytes and pericytes

To generate a fully iPSC-derived human neurovascular unit (NVU), we integrated rBMECs, iPSC-derived astrocytes (iACs), and iPSC-derived pericytes (iPCs) into a 3D commercial microfluidic chip platform (**Fig. 4A**). The MIMETAS OrganoPlate® is comprised of three lanes, in which brain endothelial cells in the "blood" channel form a tubule against a collagen gel in the "ECM" channel[65,66]. iACs and iPCs (**Fig. S4A-F**) are introduced in the "brain" channel and migrate towards the blood channel to contact the endothelial tubule. rBMECs were able to form continuous tubules at 10 days after seeding (**Fig. 4B)**. These rBMEC tubules stained positive for endothelial markers CD31 and VE-cadherin and tight junction markers CLDN5 and ZO-1 (**Fig. 4C).** In rBMECs cocultured with iACs and iPCs, we observed ZO-1 staining colocalizing with astrocyte marker S100β and pericyte marker PDGFRβ, suggesting that iACs and iPCs migrated across the ECM channel to contact the rBMEC tubule **(Fig. 4D-E).** Next, we performed tracer experiments utilizing a small ~900Da Biocytin tracer and a 70kDa dextran tracer. We introduced tracers into the blood channel, allowed them to diffuse across to the other side, and measured the fluorescent signal in the middle channel to evaluate the leakage of tracers through the tubule. We found that rBMECs exhibited decreased leakage of both Biocytin and 70kDa dextran compared to primary HBMECs, suggesting that they had higher paracellular and transcellular barrier tightness (**Fig. 4F-H**). rBMECs cocultured with iACs and iPCs exhibited even lower permeability to the smaller tracer Biocytin compared to rBMECs alone by 45 minutes, suggesting greater paracellular tightness **(Fig. 4H**). Finally, we performed TEER analysis utilizing the commercial OrganoTEER instrument from MIMETAS[65]. While considerable variability existed between experiments, rBMECs cocultured with iACs/iPCs had elevated TEER compared to rBMECs alone, which overall was higher than that of HBMECs alone (**Fig. 4I, S4G**). Therefore, rBMECs form stable and continuous tubules in the MIMETAS microfluidic system with decreased permeability to fluorescent tracers and increased TEER compared to primary HBMECs. Overall, rBMECs maintain endothelial identity and angiogenic potential, exhibit a high barrier tightness and BBB-like molecular properties, and respond to an AD-relevant pathogenic stimulus. rBMECs thus have great utility as an endothelial source for iPSC-based 3D NVU models of BBB function and CNS disease.

DISCUSSION

Here, we describe a novel method of generating bona fide iPSC-derived BMECs using transcriptional reprogramming of BBB-primed endothelial cells (bpECs) via lentiviral overexpression of FOXF2 and ZIC3. rBMECs express key BBB markers at the protein (**Fig. 1**) and transcript levels (**Fig.**

2) and lack markers for epithelial identity (**Fig. S1B**). Angiogenesis can be induced by addition of angiogenic factors (**Fig. 1J-K**), and rBMECs can be activated by addition of oAβ42 (**Fig. 3H-M**). rBMECs have reduced caveolae-mediated transcytosis as measured by uptake of fluorescent BSA and increased efflux of rhodamine 123 compared to primary HBMECs. Importantly, they exhibit high TEER compared to bp-ECs and primary HBMECs, suggesting that rBMECs have decreased paracellular transport (**Fig. 3A-B**). To create a more physiological model, we also incorporated rBMECs, iACs, and iPCs into a 3D-microfluidic NVU using the MIMETAS platform (**Fig. 4**). hiPSC-derived NVUs have lower permeability to a small tracer, Biocytin, and increased TEER compared to NVUs derived from primary human HBMECs, astrocytes, and pericytes. Overall, our rBMECs can be utilized as an *in vitro* human-specific BBB monolayer model and 3D microfluidic NVU model.

To generate rBMECs, we transdifferentiated bpECs with FOXF2 and ZIC3. bpECs were originally described as precursors for brain capillary-like endothelial cells that became more BBB-like when treated with a VEGF/Wnt3A/RA cocktail[46]. These cells have some BBB properties, such as expression of claudin-5 and Occludin (**Fig. 1E-F**) and TEER equivalent to that of primary HBMECs (**Fig. 3A-B**). They appear particularly amenable to acquiring stronger BBB properties by FOXF2 and ZIC3 transduction, as our initial efforts to transduce a different endothelial progenitor cell (EPC)[67] or ECs generated by a commercial kit (StemCell Technologies) with FOXF2 and ZIC3 failed to result in significantly elevated barrier properties as measured by TEER (data not shown). The precise mechanism by which bpECs are predisposed to a BBB fate remains unclear and should be the focus of future studies. It should also be noted that although the original study using these bpECs had benefits in barrier function from the addition of Wnt3A, activation of Wnt signaling via treatment with CHIR99021 did not further increase rBMEC TEER in multiple experiments (data not shown).

Ultimately, the goal of this study was to develop an improved *in vitro* human BBB model that could be applied to study pathogenic mechanisms and develop therapeutics for a variety of neurodegenerative and neurological disorders by the broader research community. We began modeling efforts by assessing the effect of oAβ42 on barrier integrity and endothelial activation. Interestingly, oAβ42 did not directly affect barrier tightness as measured by TEER but did lead to transcriptional upregulation of pro-inflammatory cytokines and endothelial activation genes, including VCAM-1 and ICAM-1 (**Fig. 3H-M**). This suggests that oAβ42 does not simply damage the BBB to cause dysfunction, but rather serves as an immune signaling molecule, consistent with the antimicrobial protection hypothesis of AD[68]. This contrasts with damaging aggregated fibrillar forms of Aβ seen in cerebral amyloid angiopathy (CAA)[69]. Future studies will determine if oAβ42 is sufficient to recruit peripheral

monocytes and potentially T cells across the BBB, and the potential role of AD-specific genetic risk factors in this process and for overall BBB function.

Limitations of the study

While rBMECs have BBB functional properties and molecular identity, they do not fully recapitulate all aspects of the BBB. For instance, they do not robustly express the full repertoire of BBB-specific transporters such as MSFD2A. Perhaps addition of relevant substrates to the media (i.e. lipids) may overcome this deficit in future iterations of the protocol. In addition, one major drawback of this differentiation strategy is the very low efficiency to produce bpECs (Sort A). Unfortunately, attempts to transdifferentiate ECs generated from other higher yield protocols failed to produce cells with robust barrier properties. Further optimization of the existing bpEC protocol might be able to increase the efficiency in the future. Finally, we do not fully understand the precise mechanisms by which FOXF2 and ZIC3 increase BBB properties in bpECs, which should be investigated in future studies. It should also be noted that although multiple lots of HBMECs from two independent sources were used for comparison with bpECs and rBMECs, other groups have reported better properties of these cells in some cases, which likely reflects improved individual lots.

Acknowledgements: We would like to thank Raphael Lis for providing FOXF2 and ZIC3 expression plasmids which were used as a template for subcloning, and Paroma Malick in Alex Chavez's lab for subcloning FOXF2 and ZIC3 into pLEX_307. Flow cytometry and cell sorting experiments were performed in the Columbia Stem Cell Initiative Flow Cytometry core facility at Columbia University Irving Medical Center under the leadership of Michael Kissner. This work was supported by NIH grants R33/ R61HL159949-01 (DA PI, AAS Co-I) and RF1AG078352 (MPI AAS, DA). AC, UA, and DA are also supported by grants from the National Eye Institute (R01EY033994), National Institute of Neurological Disorders and Stroke (R21NS130265), the National Multiple Sclerosis Society (RG-1901-33218, and in part by a gift donation. AAS is also supported by the Henry and Marilyn Taub Foundation and Thompson Family Foundation (TAME-AD).

Author contributions: RP, AC, and PB contributed equally to this work, which included conceptualizing, planning, conducting, and interpreting experiments, as well as helping to draft the manuscript. UA led all bioinformatic analysis. ER and PBD planned and conducted experiments. AAS and DA conceptualized experiments and approaches, oversaw all work, and helped draft the manuscript. All authors edited the manuscript.

Declaration of interests: The authors declare no competing interests.

STAR* METHODS

KEY RESOURCE TABLE

REAGENT or RESOURCE	SOURCE	IDENTIFIER
Antibodies		
Goat polyclonal PDGFRbeta Antibody	R&D	Cat#AF385; RRID: AB_355339
Rabbit monoclonal anti-Vimentin antibody	Cell Signaling Technology	Cat#D21H3; RRID: AB_10695459
Mouse monoclonal Neural/Glial Antigen 2 (NG2) Antibody (9.2.27), eBioscience™	Thermo Fisher	Cat#14-6504-82; RRID: AB_10870987
Mouse monoclonal α-Smooth Muscle antibody	Sigma Aldrich	Cat#A5228; RRID: AB_262054
Mouse monoclonal Anti-Human CD31 antibody (Clone JC70A)	Agilent	Cat#M082301-2; RRID: AB_2114471
Rabbit polyclonal VE-Cadherin antibody	Abcam	Cat#ab33168; RRID: AB_870662
Rabbit polyclonal anti-GAPDH antibody	Sigma	Cat#G9545; RRID: AB_796208
Mouse monoclonal anti-S100β	Sigma-Aldrich	Cat#S2532; RRID: AB_477499
Rabbit monoclonal anti-VCAM-1	Abcam	Cat#ab134047; RRID: AB_2721053
Mouse monoclonal anti-GFAP	EMD Millipore	Cat#MAB360; RRID: AB_11212597
Rat Monoclonal anti-Ki-67 Antibody (SolA15)	Thermo Fisher	Cat#14-5698-82; RRID: AB_10854564
Mouse monoclonal anti-Claudin-5	Thermo Fisher	Cat#35-250-0; RRID: AB_2533200
Rabbit polyclonal anti-ZO-1	Thermo Fisher	Cat#61-7300; RRID: AB_2533938
Rabbit polyclonal anti-GLUT-1	Thermo Fisher	Cat#PA5-16793; RRID: AB_10986893
Mouse monoclonal anti-Occludin	Thermo Fisher	Cat#33-1500; RRID: AB_2533101
Mouse PhosphoPair STAT3 (Tyr705) Antibody Set	Biolegend	Cat.# 699952; RRIDs: AB_2861053, AB_10897947
Mouse monoclonal anti-EpCAM Direct Conjugated Antibody, Alexa Fluor 488	BioLegend	Cat#324210; RRID: AB_756084
Mouse monoclonal anti-PECAM-1 Direct Conjugated Antibody, APC	BioLegend	Cat#303116; RRID: AB_1877151
Recombinant human monoclonal anti-VE-Cadherin Direct Conjugated antibody, APC	Miltenyi Biotech	Cat#130-125-985; RRID: AB_2655162

Mouse monoclonal anti-VE-Cadherin Direct Conjugated Antibody, PE	BioLegend	Cat#348506; RRID: AB_2077978
Mouse monoclonal anti-ICAM-1 Direct Conjugated Antibody, FITC	BioLegend	Cat#353107; RRID: AB_10898317
Mouse monoclonal anti-VCAM-1 Direct Conjugated Antibody, APC	Biolegend	Cat#305809; RRID: AB_2304307
Mouse monoclonal anti-CD184 Direct Conjugated Antibody, APC	BioLegend	Cat#306509; RRID: AB_314615
Mouse monoclonal anti-CD133 Direct Conjugated Antibody, PE	BioLegend	Cat#372803; RRID: AB_2632879
Mouse monoclonal anti-CD271 Direct Conjugated Antibody, FITC	BioLegend	Cat#345103; RRID: AB_1937226
PE anti-human CD140b (PDGFRβ) Antibody	BioLegend	Cat#323605; RRID: AB_2299493
PE/Cyanine7 anti-human CD146 Antibody	BioLegend	Cat#361008; RRID: AB_2562983
Goat anti-mouse IgG (H+L), HRP conjugate	Thermo Fisher	Cat#31430; RRID: AB_228307
Goat anti-rabbit IgG (H+L), HRP conjugate	Thermo Fisher	Cat#31466; RRID: AB_10960844
Donkey anti-mouse IgG (H+L) Secondary Antibody, Alexa Fluor 488	Thermo Fisher	Cat#A21202; RRID: AB_141607
Donkey anti-mouse IgG (H+L) Secondary Antibody, Alexa Fluor 568	Thermo Fisher	Cat#A10037; RRID: AB_2534013
Donkey anti-rabbit IgG (H+L) Secondary Antibody, Alexa Fluor 568	Thermo Fisher	Cat#A10042; RRID: AB_2534017
Goat anti-rabbit IgG (H+L) Secondary Antibody, Alexa Fluor 647	Thermo Fisher	Cat#A21245; RRID: AB_2535813
Chemicals, Peptides, and Recombinant Proteins		
Recombinant human FGF-2	R&D Systems	Cat#3718-FB
Recombinant human VEGF-165	R&D Systems	Cat#293-VE-050/CF
Recombinant human VEGF-165	Stem Cells Tech.	Cat#78073.1
Recombinant human bFGF	Peprotech	Cat#100-18C-100ug
Recombinant human HGF	Peprotech	Cat#100-39H
Recombinant human Thymosinβ4	R&D Systems	Cat#3390/100U

Recombinant human BMP-4	R&D Systems	Cat#314-BP-500/CF
Recombinant β-amyloid (1-42)	rPeptide	Cat#A-1163-2
Recombinant human TNFα	R&D Systems	210-TA-020/CF
Recombinant human IL-1β	R&D Systems	201-LB-005/CF
Human transferrin	Sigma-Aldrich	Cat#T3309
Collagen from human placenta, type IV	Sigma-Aldrich	Cat#C5533
Fibronectin from human plasma	Sigma-Aldrich	Cat#F2006
Cultrex Stem Cell Qualified RGF Basement Membrane	R&D	Cat#3434-010-02
Insulin solution	Sigma-Aldrich	Cat#19278
Puromycin	Sigma-Aldrich	Cat#P8833
Poly-D-Lysine	MP Biomedicals	Cat#0215017510
SB 431542	Selleck Chemicals	Cat#S1067
CHIR 99021	Tocris	Cat #4423
Collagenase Type IV	StemCell Technologies	Cat#07909
Plasma derived-platelet poor serum	Sigma-Aldrich	Cat#P2918
Knockout serum replacement	Thermo Fisher	Cat#10828028
Fetal Bovine Serum, heat-inactivated	Sigma Aldrich	Cat#12306C
Bovine serum albumin	Sigma-Aldrich	Cat#A9576
Bovine serum albumin	Sigma-Aldrich	Cat#A9418
Accutase	Thermo Fisher	Cat#A11105-01
ReleSR	StemCell Technologies	Cat#100-0483
Trypsin-EDTA (0.05%)	Thermo Fisher	Cat#25300-054
β-mercaptoethanol	Thermo Fisher	Cat#21985-023
GlutaMAX	Thermo Fisher	Cat#35050-061
MEM non-essential amino acids	Thermo Fisher	Cat#11140-050
Penicillin-streptomycin (10,000 U/mL)	Thermo Fisher	Cat#15140-122
B-27 Supplement, minus vitamin A	Gibco	Cat#12-587-010
N-2 Supplement	Gibco	Cat#17502048
Rhodamine 123, FluoroPure™ grade	Invitrogen	Cat#R22420
Albumin from Bovine Serum (BSA), Alexa Fluor™ 594 conjugate	Invitrogen	Cat#A13101
PSC-833	Tocris	Cat#4042
SuperBlock Blocking Buffer in PBS	Thermo Fisher	Cat#37515
Triton-X	Thermo Fisher	Cat#A16046
Tween 20	Thermo Fisher	Cat#BP337

SuperBlock T20 Blocking Buffer	Thermo Fisher	Cat#37536
CF® Dye Biocytin CF640	Biotium	Cat#92007
70,000 MW Dextran CF770	Biotium	Cat##80123
CellTag 700 Stain	LI-COR	Cat#926-41090
eBioscience Fixable Viability Dye eFluor 780	Thermo Fisher	Cat#65-0865-14
Critical commercial assays		
BCA Protein Assay Kit	Millipore Sigma	Cat#71285-3
SuperSignal West Pico PLUS Chemiluminescent Substrate	Thermo Fisher	Cat#34577
RNeasy Mini Kit	Qiagen	Cat#74104
RNeasy Micro Kit	Qiagen	Cat#74004
Maxima First Strand cDNA Synthesis Kit for RT-qPCR	Thermo Fisher	Cat#K1642
Lipofectamine 3000 Transfection Kit	Thermo Fisher	Cat#L3000001
Human endothelial serum-free media	Gibco	Cat#11111044
Endothelial Cell Growth Medium MV2	PromoCell	Cat#C-22121
Astrocyte Medium Kit	ScienCell	Cat#1801
Pericyte Medium Kit	ScienCell	Cat#1201
F-12, phenol red free	R&D	Cat#M25350
DMEM / F12 (1:1)	Gibco	Cat#11320-033
F12	Gibco	Cat#11765-054
IMDM	Gibco	Cat#12440-053
DMEM	Gibco	Cat#11965-092
Knockout DMEM	Gibco	Cat#10829-018
Experimental Models: Cell lines		
HEK293T	ATCC	Cat#CRL-1573
Irradiated CF1 mouse embryonic fibroblasts	Thermo Fisher	Cat#A34181
Primary Human Umbilical Vein Endothelial Cells	ATCC	Cat#PCS-100-010
Primary Human Brain Microvascular Cells	Cell System	Cat#ACBRI376
Human Brain Vascular Pericytes	ScienCell	Cat#1200
Human Astrocytes	ScienCell	Cat#1800
iPS(IMR90)-4	WiCell	RUID# WISCi004-B
FA0000010 (FA10)	RUCDR	RUID# CUIMCi001-A
ND50031 (NCRM-5)	RUCDR/NINDS Collection	RUID#CR0000005, Clone ID: R149506778

Oligonucleotides		
Primers for RT-qPCR: listed in Supplementary Table A		
Recombinant DNA		
FOXF2 lentiviral construct	This manuscript	Backbone: Addgene_41392
ZIC3 lentiviral construct	This manuscript	Backbone: Addgene_41392
NFIA lentiviral construct	Addgene	Backbone: Addgene_141403
Software and Algorithms		
ImageJ	NIH	https://imagej.nih.gov/ij/
FlowJo	FLOWJO LLC	https://www.flowjo.com/
GraphPad Prism 9.0.0	GraphPad Software Inc.	https://www.graphpad.com/features
R studio v2023.12.0+369	R Studio	R Studio
EdgeR package 2.1	BioConductor	https://github.com/alexdobin/STAR
STAR Alligner v2.5.2a	Dobin et al. 2013. STAR: ultrafast universal RNA-seq aligner. Bioinformatics 29(1):15-21.	
FastQC	Babraham Institute	http://www.bioinformatics.babraham.ac.uk/projects/fastqc/
subread	https://academic.oup.com/nar/article/41/10/e108/1075719?login=false	https://subread.sourceforge.net/
Zen 3.9	Zeiss Company	https://www.zeiss.com/microscopy/en/products/software/zeiss-zen.html

Resource availability

For further information and requests for resources, reagents, or code, please contact corresponding authors Andrew Sproul (aas2003@cumc.columbia.edu) and Dritan Agalliu (da191@cumc.columbia.edu).

Materials availability

Plasmids from this study are available upon reasonable request. Please refer to STAR*Methods section for resources.

Experimental Models

Human iPSC line maintenance: For all primary experiments, human control iPSC line IMR90-cl.4 was used (WiCell)[70]. For additional experiments, human control iPSC line FA0000010 (RUCDR) and NCRM-5 (NIH CRM control iPSC line, NIH) were used. IMR90-cl.4 was derived from a female donor, while FA000010 and NCRM-5 were from male donors. For differentiation into bpECs or NPCs, iPSCs were maintained on feeder culture of irradiated CF1 mouse embryonic fibroblasts (MEFs) with Human Embryonic Stem cell Medium (HUESM): knockout DMEM, 20% knockout serum replacement (Thermo Fisher), 2mM Glutamax (Thermo Fisher), 0.1 mM MEM non-essential amino acids (Thermo Fisher), 1% penicillin-streptomycin (Thermo Fisher), and 0.1 mM β-mercaptoethanol (Thermo Fisher) supplemented with 20 ng/mL bFGF (R&D) and passaged when 80-90% confluent. Feeder-free hiPSCs were maintained in StemFlex medium (Thermo Fisher) containing penicillin-streptomycin (Thermo Fisher) on Cultrex-coated plates (Bio-Techne). Cultures were passaged using ReLeSR (StemCell Technologies) every 3-4 days. Standard mycoplasma testing was performed using a PCR-based kit (Bulldog-Bio).

Directed differentiation of hiPSCs into BBB-primed endothelial cells (bpECs): hiPSCs were differentiated into bpECs as previously reported with slight modifications[46]. hiPSCs were dissociated with collagenase-IV, and cell aggregates were plated in chemically defined media (CDM): 50% IMDM (Thermo Fisher), 50% Ham's F12 (Thermo Fisher), 5 mg/mL bovine serum albumin (Thermo Fisher), 15 ug/mL transferrin (Sigma-Aldrich), 0.1 mM β-mercaptoethanol (Thermo Fisher), 7 ug/mL insulin (Sigma-Aldrich), 1% penicillin-streptomycin (Thermo Fisher) on 1 ug/mL fibronectin (Sigma-Aldrich) coated 10 cm dishes from one well of a 6-well plate to one 10 cm dish. CDM was supplemented with 10 ng/mL BMP4 (R&D) for 1.5 days to induce mesodermal differentiation and 50 ng/mL BMP4 and 20 ng/mL bFGF (R&D) for the next 3.5 days for further expansion of mesodermal lineage cells. From days 5 to 10, endothelial differentiation was initiated by supplementing CDM media with 50 ng/mL VEGF (R&D) and 100 ng/mL thymosin-β4. Endothelial cells were purified at day 10-11 by FACS for $CD31^+/CDH5^+$ cells. These endothelial cells, now termed bpECs, were plated on collagen IV/fibronectin coated plates at a density of 30,000 to 35,000 cells/cm^2 and fed EC medium (Human Endothelial Serum

Free Medium (Thermo Fisher) supplemented with 1% human serum (Sigma-Aldrich) supplemented with 50 ng/mL VEGF165 (R&D), 20 ng/mL bFGF (R&D), and 10 μM SB431542 (Sigma-Aldrich). bpECs were expanded and passaged 1:2 to 1:3 every 7-10 days and generally used for five passages.

Reprogramming of bpECs into rBMECs: bpECs were plated at 30,000-35,000 cells/cm^2 on collagen IV/fibronectin coated plates using EC media supplemented with 50 ng/mL VEGF165, 20 ng/mL bFGF and 10 uM SB431542. On day 2, bpECs were transduced with FOXF2 (~1x10^6 lentiviral p24 units/mL of medium) determined by Lenti-X GoStix (Takara) and ZIC3 (~7.5x10^5 lentiviral p24 units/mL of medium) determined by Lenti-X GoStix. Successfully infected cells were selected with 1 ug/mL puromycin (Sigma) for 24 to 48 hours. Infected bpECs were purified via FACS for CD31$^+$/VE-cadherin$^+$ cells on day 14. FACS-purified and infected bpECs, referred to as rBMECs, were plated on collagen IV/fibronectin coated plates 25,000-35,000 cells/cm^2 and expanded until confluent. rBMECs were passaged at high density using 1:2 splits every 7-10 days and used within five passages.

Generation of lentiviral vectors and lentiviruses: FOXF2 and ZIC3 were subcloned into pLex_307, which was a gift from David Root (Addgene), and verified by Sanger sequencing (Azenta). FUW-tetO-NFIA was a gift from Lorenz Studer (Addgene)[71]. FUdeltaGW-rtTA was a gift from Konrad Hochedlinger (Addgene)[72]. psPAX2 was a gift from Didier Trono (Addgene). VSV.G was a gift from Tannishtha Reya (Addgene)[73]. Lentiviral particles for FOXF2, ZIC3, NFIA, and rtTA were generated in HEK293 as described previously[74], using the psPAX2/VSV.G 2nd generation system. Efficacy of lentiviral particles was confirmed by infection and titered using qPCR.

Fluorescence-activated cell sorting (FACS): Cells were dissociated into single cell suspension using Accutase (ThermoFisher) and washed with base medium (CDM for EC differentiation at day 10 and EC media for rBMECs). Cell suspensions were incubated with FACS buffer (10% KOSR in DPBS) with fluorescently tagged antibodies (CD31-FITC, VE-cadherin-APC) for 30 min at room temperature protected from light. Cell suspensions were washed with FACS buffer and cell pellets were resuspended for FACS by filtering through 0.45 μM filters (Fisher Scientific) to remove cell aggregates. bpECs or rBMECs were sorted on the Sony MA900 cell sorter and double positive CD31$^+$/VE-cadherin$^+$ cells were subsequently expanded.

Primary endothelial cell, pericyte, and astrocyte cultures: HBMECs (Cell Systems) were cultured in Endothelial Cell Growth Medium MV 2 (Promocell). PCs were cultured in Pericyte Media (PM,

ScienCell), and ACs were cultured in Astrocyte Media (AM, ScienCell). HBMECs and PCs were plated onto collagen IV and fibronectin coated plates, while ACs were plated onto either Matrigel or Cultrex-coated plates. All cells were supplemented with media every other day and passaged using Accutase once 90% confluent.

Generation of iPSC-derived pericytes: Briefly, feeder-free iPSCs were differentiated into neural crest pericytes following an established protocol, where iPSCs were treated with a neural crest differentiation media supplemented with CHIR99021 and subsequently treated with Pericyte Media (ScienCell)[75]. Cells were later sorted on CD146+/PDGFRβ+ to ensure a homogeneous population prior to introduction into the BBB triculture system.

Generation of iPSC-derived astrocytes: hiPSCs were differentiated into a neural progenitor cells (NPCs) using dual-SMAD inhibition in embryoid bodies as previously described[76]. On day -1, NPCs were dissociated using Accutase and plated at a density of 15,000 cells/cm^2 in N2/B27 media on Cultrex-coated plates. On day 0, the media was replaced with supplemented Astrocyte Media (2% fetal bovine serum, and proprietary astrocyte growth factor supplement) (ScienCell). On day 1, differentiating cells were transfected with lentiviral particles carrying dox-inducible NFIA and rtTA (Addgene). Cells were fed every other day using astrocyte media supplemented with doxycycline (2μg/mL) (Sigma-Aldrich). Cells were split at 90-95% confluence roughly once every seven days and re-plated at a density of 15,000 cells/cm^2 for 30 days. At this stage, astrocytes were split 1:3 once 90-95% confluent and were expanded, banked, and utilized.

RNA isolation and RT-qPCR: RNA was extracted using the RNeasy Plus Micro Kit (Qiagen) and resuspended in 30 μl of RNAse-free water. RNA quantity and quality were assessed with a Nanodrop One (ThermoScientific). For qPCR, 100-250 ng of RNA was transcribed into cDNA using the Maxima First Strand cDNA Synthesis Kit (Thermo Fisher). Gene expression was assessed using the FAST SYBR Green Master Mix (ThermoFisher Scientific) with primer sets (Integrated DNA Technologies) for target genes on a QuantStudio 7 Flex system (Applied Biosystems) and CFX Opus 384 (Bio-Rad). Gene expression for target genes were normalized to GAPDH and fold changes were calculated as $\Delta\Delta C_t$.

Western blotting: Endothelial cells were harvested using RIPA Lysis Buffer supplemented with Halt protease and phosphatase inhibitors single-use cocktails (Thermo Fisher) on ice. 10 μg of lysates and 1x

Laemmli sample buffer/5% β-mercaptoethanol were boiled at 95° C for 5 min. SDS-PAGE was performed by loading samples on Bolt 4–12% gradient Bis-Tris gels using Bolt MOPS buffer (Thermo Fisher). Nitrocellulose membranes were first blocked with Superblock TBS buffer/0.1% Tween 20 Thermo Fisher) for 1h, and then incubated overnight at 4° C with the following primary antibodies diluted in Superblock/0.1% Tween 20: Claudin-5 (1:1000; Thermo Fisher), Occludin (1:1000; Thermo Fisher), VCAM-1 (1:1000, Abcam), pSTAT3 (1:1000, BioLegend), STAT3 (1:1000, BioLegend) and GAPDH (1:5000; Thermo Fisher). After 3 washes with TBS/0.1% Tween-20, membranes were then incubated with the appropriate HRP-conjugated secondary antibody (1:5000, Thermo Fisher) for 1 hour, and washed 3 more times with TBS/0.1% Tween-20. Pierce ECL western blotting substrate or super signal west pico plus chemiluminescent substrate (Thermo Fisher) were used to develop chemiluminescence and blots were imaged using the Bio-Rad Chemidoc MP system.

Transendothelial electrical resistance (TEER) measurement: TEER measurements were carried out using THE ECIS Z-theta instrument on the 96W20idf array at 4000 Hz frequency. Briefly, 20,000 cells were plated on poly-D-lysine and collagen IV/fibronectin-coated 96-well electrode array plates in the respective medium for each cell type. Resistance was recorded for 250-300 hours and medium was changed every other day. The resistance curve was generated using PRISM (Graphpad) and the area under the curve (AUC) was measured either for last 100 hours of recording or for the duration of oAβ42 or cytokine treatment (72hr or 24hr) using the AUC PRISM function.

Wound scratch assay: Cells were plated at a density of 100K/well (24-well plate). Once confluent, cells were fed their standard media absent VEGF and bFGF supplementation. Monolayers were scratched in the center of each well using the Autoscratch automated scratch machine (BioTek). Wells were then treated with either control media, 100 ng/mL VEGF, or an angiogenic cocktail consisting of VEGF (37.5 ng/ml), bFGF (37.5 ng/ml), and HGF (37.5 ng/ml). Plates were cultured in imaged automatically every 6 hours using the Cytation5 plate reader (BioTek) and software for HBMECs (24 hrs) and bpECs and rBMECs (36 hrs) during culture in a BioSpa incubator (BioTek). Each well was quantified for % surface area of the wound utilizing an ImageJ plug-in for identifying the area of the scratch[77], which was then normalized to the original size of the wound for each well. To compare cell types, we calculated an angiogenic potential, where:

$$\text{angiogenic potential} = \int \text{untreated wound area} - \int \text{wound area with angiogenic cocktail}$$

Ki67 quantification assay: After the wound scratch assay was performed, cells were fixed with 4% PFA. Cells were blocked as described above and stained with Ki67 antibody (1:500). Cells were labeled with a GFP secondary antibody and DAPI. Wells were imaged for DAPI and GFP fluorescence on the BioSpa as done previously. Each well was quantified for proliferative index, where:

$$\text{Proliferative Index} = \frac{\text{Number of Ki67+ cells}}{\text{Number of DAPI+ cells}}$$

Cells were identified as Ki67 or DAPI positive using the annotation machine learning tool from the QuPath software.

Uptake and transporter assays: As previously described[14], cells were plated at a density of 100K/well (24-well plate) and subcultured until confluent. First, cells incubated with either 1 mg/mL unlabeled BSA or 1 mg/mL BSA-Alexa 594 for 1 hour at 37º C. Cells were then dissociated into single cell suspension, fixed with 4% PFA, and analyzed for Alexa594 median fluorescence intensity (MFI). For the transporter assay, cells were incubated with Rhodamine 123 (10 uM) for 1 hr at 37º C. To assess the effect of P-glycoprotein (Pgp) efflux, cells were pretreated with PSC-833 (a specific Pgp inhibitor) for 1 hr prior to Rhodamine treatment. Cells were dissociated into single cell suspension, fixed with 4% PFA, and analyzed for Rhodamine MFI. NPCs were utilized as a positive control due to their low level of Pgp efflux. Data were normalized to the unstained MFI for each cell type, which we termed fold change in MFI. To calculate Pgp efflux, we calculated the percent change in MFI with and without PSC-833:

$$\text{PGP efflux} = \frac{\text{MFI}_{\text{PSC-833}} - \text{MFI}_{\text{Rhodamine}}}{\text{MFI}_{\text{Rhodamine}}}$$

Amyloid-β42 oligomerization and treatment: Amyloid-β42 was monomerized, stored and later oligomerized as previously described[78,79]. In brief, Aβ(1-42) (rPeptide, 1 mg) vial was allowed to equilibrate to room temperature. Peptides were resupended in ice-cold hexafluoroisopropanol (Sigma-Aldrich) to achieve 1 mM concentration directly in a vacuum-sealed vial using a Hamilton syringe. The suspension was divided into 8 equal aliquots by volume using a Hamilton syringe into low protein binding Eppendorf tubes, incubated at room temperature for 2 hours and dried on speedvac at 800g for 25°C. Upon drying monomerized Aβ(1-42) films can be stored at -80°C in sealed tubes. For generating oligomers, Eppendorf tubes containing Aβ(1-42) peptide films were equilibrated to room temperature,

resuspended in DMSO to achieve 5 mM concentration and sonicated at 17°C for 10 min for complete resuspension. Oligomerization was induced by adding phenol-red free F12 to achieve final concentration of 100 uM and incubated at 4°C for 24 to 48 hours. rBMEC monolayers were treated with oAβ at 500 nM or 1 uM concentrations for the indicted period of time and F12 was used a vehicle control.

3D microfluidic BBB culture model: OrganoPlate 3-lane-64 plates (MIMETAS) were used to generate a 3D microfluidic system of the BBB. In each chip, the center channel was filled with an ECM gel, an endothelial tubule was generated in the right channel, and a mixture of iPSC-derived astrocytes and pericytes was seeded in the left channel and allowed to migrate towards the endothelial cells during culture upon a bidirectional OrganoFlow rocker (MIMETAS).

ECM generation and endothelial channel coating: On day -1, the center ECM channel was filled with a 4:1 ratio of collagen I (5 mg/ml) and collagen IV solution (5 mg/mL), incubated at 37º C for 15 min, and covered with PBS to prevent collagen gel from drying. The right channel inlet was coated using fibronectin (10 ug/mL) and collagen IV (10 ug/mL) overnight.

Endothelial cell seeding: On day 0, endothelial cells were singularized and resuspended to achieve a 15,000 cells/uL concentration. Cells were seeded in the right channel outlet at a density of 30,000 cells/chip. Plate was placed on a 75º plate stand from the manufacturer and incubated at 37º C for four to five hours to allow endothelial cells to settle against the gel. Then, outlets were replenished with endothelial media and the plate was placed on the OrganoFlow rocker to alternate between -7 to +7° every 8 minutes. After a day or two, endothelial cells formed an open tubule in the right channel.

Astrocyte and pericyte channel coating and cell seeding: On day 1, the left channel inlet was coated with Matrigel in DMEM. Primary astrocytes (ACs) and iPSC-derived ACs were singularized and resuspended in AM-PM media (2:1 ratio of AM:PM) to achieve a 15,000 cells/uL concentration. Primary pericytes (PCs) and iPSC-derived iPCs were similarly singularized and resuspended in AM-PM to achieve a 7,500 cells/uL concentration. Primary astrocytes and primary pericytes were mixed at a ratio of 1:1 and seeded in the left channel outlet for each chip to achieve 15,000 ACs and 7,500 PCs per chip. The plate was rested on the stand for four to five hours at 37º C to allow pericytes and astrocytes to settle against the gel. Finally, outlets were replenished with AM-PM and the plate was placed back on the OrganoFlow rocker for continuous culture until Day 10. Media was replenished every other day.

Beginning on day 6, chips were replenished with their standard EC media without bFGF and VEGF supplementation.

Tracer permeability assay: On day 10 post seeding, a 70-kDa dextran (0.5 ug/mL) and Biocytin tracer (0.5 ug/mL) were introduced into the right inlet and outlet wells (40 uL and 30 uL, respectively). The gel inlet, left inlet, and left outlet wells were filled with 20 uL media without tracer. Then, the plate was placed onto the OrganoFlow rocker and imaged every 15 minutes in the LI-COR. The fluorescence intensity for each well was quantified with the Odyssey SA system. Analysis was performed as the normalized fluorescence intensity over the ECM channel center well, which represented the leakage from the right vascular channel into the left brain channel:

$$\text{Normalized Intensity} = \frac{\text{Middle ECM channel intensity}_{\text{sample}}}{\text{Mean middle channel intensity}_{\text{ECM}}}$$

where ECM chips only had a control gel, representing the leakage without cells present. Samples were analyzed using a two-way ANOVA test.

3D TEER assay: Chips were assayed for TEER on day 10. Post seeding After the plate was introduced into the OrganoTEER device, TEER values were measured for the vascular channel using the “low TEER” setting, which is suitable for endothelial cells, per the manufacturer. Measurements for each condition were compared using a one-way ANOVA test.

Immunofluorescence and microscopy

Staining of monolayer endothelial cells, pericytes, and astrocytes: For tight junction staining, endothelial cells were fixed with ice cold ethanol for 30 minutes and acetone for 1 minute. For all other staining, ECs, PCs, and ACs were fixed in 4% PFA for 15 min. Fixed monolayers were then washed twice in PBS, blocked for an hour in blocking buffer (5% goat or donkey serum, 0.3% Triton X-100 in PBS), and incubated overnight with appropriate primary antibodies in a diluting solution at 4º C (5% goat or donkey serum; 0.01% Triton X-100 in 1 x PBS). The following day, cells were stained with secondary antibodies in 1 x PBS for 1 hour at room temperature and DAPI (1:5000) for 10 minutes. Imaging was performed on a ZEISS LSM700 confocal microscope using 10x (Plan-Apochromat 10x objective lens) and 20x (Plan Apochromat 20x objective lens).

Immunostaining of 3D MIMETAS cultures: On day 10 post seeding, MIMETAS chips with fixed with either 4% PFA for 15 minutes for standard staining or ethanol/acetone for tight junction visualization. For fixation and blocking, solution was introduced as follows: 100 uL in right channel inlet, 50 uL in right channel outlet, 50 uL in left channel inlet, 50 uL in left channel outlet. Plate was placed on the OrganoFlow for rocking during staining. Chips were blocked for an hour in blocking buffer, and incubated overnight with primary antibodies in diluting solution at 4º C as follows: 25 uL in right channel inlet and outlet; 15 uL in left channel inlets and outlets. Cells were washed and incubated with secondary antibodies and DAPI as above. Then, chips were post-fixed with 4% PFA for 15 minutes prior to microscopic imaging.

Bulk RNA sequencing, alignment and analysis:

Total RNA was extracted as previously described. RNA samples underwent quality assessment using the Qubit 2.0 Fluorometer, and RNA integrity was assessed using the Agilent TapeStation 4200. Subsequently, RNA sequencing libraries were prepared using the NEBNext Ultra II RNA Library Prep Kit following the manufacturer's protocol. The samples were sequenced in a 2x150bp Paired-End (PE) configuration using the Illumina NovaSeq instrument.

Previously published samples were obtained from Gene Expression Omnibus (GEO) datasets, including GSE138025, GSE40291, GSE57662, GSE131039, GSE97575, GSE73721, GSE97324, GSE138025, GSE122588, GSE129290, GSE97100, GSE126449, GSE108012, GSE151976, GSE85403, GSE82207, GSE77250, GSE82207, GSE157852, GSE243193, GSE225549, and GSE227501. Quality control for the samples was conducted using FastQC, followed by adapter trimming with Skewer (v0.2.2). The resulting reads were aligned to the human reference genome (hg38) using the STAR aligner, and counts were generated using subread.

Normalization was performed using the trimmed mean of M-values (TMM) method implemented in the EdgeR R package. Fragments per kilobase of transcript per million mapped reads (FPKM) and Log2 counts per million (cpm) matrices were generated to account for library size variations. Differential expression analysis was conducted considering a p-adjusted value < 0.05 and a log2fold change less than -0.5 or greater than 0.5.

Principal component analysis and Pearson correlation values were computed using the resulting Log_2 cpm values. Heatmaps were generated using Min-Max scaling on normalized counts.

REFERENCES

1. Eelen, G., de Zeeuw, P., Simons, M., and Carmeliet, P. (2015). Endothelial cell metabolism in normal and diseased vasculature. Circ Res *116*, 1231-1244. 10.1161/circresaha.116.302855.
2. Liebner, S., Dijkhuizen, R.M., Reiss, Y., Plate, K.H., Agalliu, D., and Constantin, G. (2018). Functional morphology of the blood–brain barrier in health and disease. Acta Neuropathologica *135*, 311-336. 10.1007/s00401-018-1815-1.
3. Marchetti, L., and Engelhardt, B. (2020). Immune cell trafficking across the blood-brain barrier in the absence and presence of neuroinflammation. Vascular Biology *2*, H1-H18. 10.1530/vb-19-0033.
4. Profaci, C.P., Munji, R.N., Pulido, R.S., and Daneman, R. (2020). The blood–brain barrier in health and disease: Important unanswered questions. Journal of Experimental Medicine *217*. 10.1084/jem.20190062.
5. Abadier, M., Haghayegh Jahromi, N., Cardoso Alves, L., Boscacci, R., Vestweber, D., Barnum, S., Deutsch, U., Engelhardt, B., and Lyck, R. (2015). Cell surface levels of endothelial ICAM-1 influence the transcellular or paracellular T-cell diapedesis across the blood-brain barrier. Eur J Immunol *45*, 1043-1058. 10.1002/eji.201445125.
6. Knowland, D., Arac, A., Sekiguchi, Kohei J., Hsu, M., Lutz, Sarah E., Perrino, J., Steinberg, Gary K., Barres, Ben A., Nimmerjahn, A., and Agalliu, D. (2014). Stepwise Recruitment of Transcellular and Paracellular Pathways Underlies Blood-Brain Barrier Breakdown in Stroke. Neuron *82*, 603-617. 10.1016/j.neuron.2014.03.003.
7. Lutz, S.E., Smith, J.R., Kim, D.H., Olson, C.V.L., Ellefsen, K., Bates, J.M., Gandhi, S.P., and Agalliu, D. (2017). Caveolin1 Is Required for Th1 Cell Infiltration, but Not Tight Junction Remodeling, at the Blood-Brain Barrier in Autoimmune Neuroinflammation. Cell Reports *21*, 2104-2117. 10.1016/j.celrep.2017.10.094.
8. Montagne, A., Zhao, Z., and Zlokovic, B.V. (2017). Alzheimer’s disease: A matter of blood–brain barrier dysfunction? Journal of Experimental Medicine *214*, 3151-3169. 10.1084/jem.20171406.
9. Sweeney, M.D., Sagare, A.P., and Zlokovic, B.V. (2018). Blood-brain barrier breakdown in Alzheimer disease and other neurodegenerative disorders. Nat Rev Neurol *14*, 133-150. 10.1038/nrneurol.2017.188.
10. Sweeney, M.D., Zhao, Z., Montagne, A., Nelson, A.R., and Zlokovic, B.V. (2019). Blood-Brain Barrier: From Physiology to Disease and Back. Physiol Rev *99*, 21-78. 10.1152/physrev.00050.2017.
11. Zenaro, E., Piacentino, G., and Constantin, G. (2017). The blood-brain barrier in Alzheimer's disease. Neurobiol Dis *107*, 41-56. 10.1016/j.nbd.2016.07.007.
12. Drouin-Ouellet, J., Sawiak, S.J., Cisbani, G., Lagacé, M., Kuan, W.L., Saint-Pierre, M., Dury, R.J., Alata, W., St-Amour, I., Mason, S.L., et al. (2015). Cerebrovascular and blood-brain barrier impairments in Huntington's disease: Potential implications for its pathophysiology. Ann Neurol *78*, 160-177. 10.1002/ana.24406.
13. Hua, J., Unschuld, P.G., Margolis, R.L., van Zijl, P.C., and Ross, C.A. (2014). Elevated arteriolar cerebral blood volume in prodromal Huntington's disease. Mov Disord *29*, 396-401. 10.1002/mds.25591.
14. Lim, R.G., Quan, C., Reyes-Ortiz, A.M., Lutz, S.E., Kedaigle, A.J., Gipson, T.A., Wu, J., Vatine, G.D., Stocksdale, J., Casale, M.S., et al. (2017). Huntington's Disease iPSC-Derived Brain Microvascular Endothelial Cells Reveal WNT-Mediated Angiogenic and Blood-Brain Barrier Deficits. Cell Rep *19*, 1365-1377. 10.1016/j.celrep.2017.04.021.
15. Trajkovic, M., Visser, T.J., Mittag, J., Horn, S., Lukas, J., Darras, V.M., Raivich, G., Bauer, K., and Heuer, H. (2007). Abnormal thyroid hormone metabolism in mice lacking the

monocarboxylate transporter 8. The Journal of Clinical Investigation *117*, 627-635. 10.1172/JCI28253.

16. Hodge, R.D., Bakken, T.E., Miller, J.A., Smith, K.A., Barkan, E.R., Graybuck, L.T., Close, J.L., Long, B., Johansen, N., Penn, O., et al. (2019). Conserved cell types with divergent features in human versus mouse cortex. Nature *573*, 61-68. 10.1038/s41586-019-1506-7.
17. Drummond, E., and Wisniewski, T. (2017). Alzheimer's disease: experimental models and reality. Acta Neuropathol *133*, 155-175. 10.1007/s00401-016-1662-x.
18. Qosa, H., Abuasal, B.S., Romero, I.A., Weksler, B., Couraud, P.O., Keller, J.N., and Kaddoumi, A. (2014). Differences in amyloid-β clearance across mouse and human blood-brain barrier models: kinetic analysis and mechanistic modeling. Neuropharmacology *79*, 668-678. 10.1016/j.neuropharm.2014.01.023.
19. Xiong, Y., Mahmood, A., and Chopp, M. (2013). Animal models of traumatic brain injury. Nat Rev Neurosci *14*, 128-142. 10.1038/nrn3407.
20. Aday, S., Li, W., Karp, J.M., and Joshi, N. (2022). An in vitro Blood-brain Barrier Model to Study the Penetration of Nanoparticles. Bio Protoc *12*, e4334. 10.21769/BioProtoc.4334.
21. Bagchi, S., Chhibber, T., Lahooti, B., Verma, A., Borse, V., and Jayant, R.D. (2019). In-vitro blood-brain barrier models for drug screening and permeation studies: an overview. Drug Des Devel Ther *13*, 3591-3605. 10.2147/dddt.S218708.
22. Linville, R.M., and Searson, P.C. (2021). Next-generation in vitro blood–brain barrier models: benchmarking and improving model accuracy. Fluids and Barriers of the CNS *18*, 56. 10.1186/s12987-021-00291-y.
23. Schreiner, T.G., Creangă-Murariu, I., Tamba, B.I., Lucanu, N., and Popescu, B.O. (2022). In Vitro Modeling of the Blood-Brain Barrier for the Study of Physiological Conditions and Alzheimer's Disease. Biomolecules *12*. 10.3390/biom12081136.
24. Fujimoto, T., Morofuji, Y., Nakagawa, S., Kovac, A., Horie, N., Izumo, T., Niwa, M., Matsuo, T., and Banks, W.A. (2020). Comparison of the rate of dedifferentiation with increasing passages among cell sources for an in vitro model of the blood–brain barrier. Journal of Neural Transmission *127*, 1117-1124. 10.1007/s00702-020-02202-1.
25. Helms, H.C., Abbott, N.J., Burek, M., Cecchelli, R., Couraud, P.-O., Deli, M.A., Förster, C., Galla, H.J., Romero, I.A., Shusta, E.V., et al. (2016). In vitro models of the blood–brain barrier: An overview of commonly used brain endothelial cell culture models and guidelines for their use. Journal of Cerebral Blood Flow & Metabolism *36*, 862-890. 10.1177/0271678x16630991.
26. Sabbagh, M.F., and Nathans, J. (2020). A genome-wide view of the de-differentiation of central nervous system endothelial cells in culture. Elife *9*. 10.7554/eLife.51276.
27. Faley, S.L., Neal, E.H., Wang, J.X., Bosworth, A.M., Weber, C.M., Balotin, K.M., Lippmann, E.S., and Bellan, L.M. (2019). iPSC-Derived Brain Endothelium Exhibits Stable, Long-Term Barrier Function in Perfused Hydrogel Scaffolds. Stem Cell Reports *12*, 474-487. 10.1016/j.stemcr.2019.01.009.
28. Lippmann, E.S., Azarin, S.M., Kay, J.E., Nessler, R.A., Wilson, H.K., Al-Ahmad, A., Palecek, S.P., and Shusta, E.V. (2012). Derivation of blood-brain barrier endothelial cells from human pluripotent stem cells. Nat Biotechnol *30*, 783-791. 10.1038/nbt.2247.
29. Qian, T., Maguire, S.E., Canfield, S.G., Bao, X., Olson, W.R., Shusta, E.V., and Palecek, S.P. (2017). Directed differentiation of human pluripotent stem cells to blood-brain barrier endothelial cells. Sci Adv *3*, e1701679. 10.1126/sciadv.1701679.
30. Vatine, G.D., Barrile, R., Workman, M.J., Sances, S., Barriga, B.K., Rahnama, M., Barthakur, S., Kasendra, M., Lucchesi, C., Kerns, J., et al. (2019). Human iPSC-Derived Blood-Brain Barrier Chips Enable Disease Modeling and Personalized Medicine Applications. Cell Stem Cell *24*, 995-1005.e1006. 10.1016/j.stem.2019.05.011.

31. Canfield, S.G., Stebbins, M.J., Morales, B.S., Asai, S.W., Vatine, G.D., Svendsen, C.N., Palecek, S.P., and Shusta, E.V. (2017). An isogenic blood-brain barrier model comprising brain endothelial cells, astrocytes, and neurons derived from human induced pluripotent stem cells. J Neurochem *140*, 874-888. 10.1111/jnc.13923.
32. Lippmann, E.S., Al-Ahmad, A., Azarin, S.M., Palecek, S.P., and Shusta, E.V. (2014). A retinoic acid-enhanced, multicellular human blood-brain barrier model derived from stem cell sources. Sci Rep *4*, 4160. 10.1038/srep04160.
33. Stebbins, M.J., Wilson, H.K., Canfield, S.G., Qian, T., Palecek, S.P., and Shusta, E.V. (2016). Differentiation and characterization of human pluripotent stem cell-derived brain microvascular endothelial cells. Methods *101*, 93-102. 10.1016/j.ymeth.2015.10.016.
34. Lu, T.M., Houghton, S., Magdeldin, T., Durán, J.G.B., Minotti, A.P., Snead, A., Sproul, A., Nguyen, D.-H.T., Xiang, J., Fine, H.A., et al. (2021). Pluripotent stem cell-derived epithelium misidentified as brain microvascular endothelium requires ETS factors to acquire vascular fate. Proceedings of the National Academy of Sciences *118*, e2016950118. doi:10.1073/pnas.2016950118.
35. Matsuo, K., Engelhardt, B., and Nishihara, H. (2023). Differentiation of Human Induced Pluripotent Stem Cells to Brain Microvascular Endothelial Cell-Like Cells with a Mature Immune Phenotype. JoVE, e65134. doi:10.3791/65134.
36. Nishihara, H., Perriot, S., Gastfriend, B.D., Steinfort, M., Cibien, C., Soldati, S., Matsuo, K., Guimbal, S., Mathias, A., Palecek, S.P., et al. (2022). Intrinsic blood-brain barrier dysfunction contributes to multiple sclerosis pathogenesis. Brain *145*, 4334-4348. 10.1093/brain/awac019.
37. Nishihara, H., Gastfriend, B.D., Soldati, S., Perriot, S., Mathias, A., Sano, Y., Shimizu, F., Gosselet, F., Kanda, T., Palecek, S.P., et al. (2020). Advancing human induced pluripotent stem cell-derived blood-brain barrier models for studying immune cell interactions. Faseb j *34*, 16693-16715. 10.1096/fj.202001507RR.
38. Gastfriend, B.D., Nishihara, H., Canfield, S.G., Foreman, K.L., Engelhardt, B., Palecek, S.P., and Shusta, E.V. (2021). Wnt signaling mediates acquisition of blood–brain barrier properties in naïve endothelium derived from human pluripotent stem cells. eLife *10*, e70992. 10.7554/eLife.70992.
39. Daneman, R., Agalliu, D., Zhou, L., Kuhnert, F., Kuo, C.J., and Barres, B.A. (2009). Wnt/β-catenin signaling is required for CNS, but not non-CNS, angiogenesis. Proceedings of the National Academy of Sciences *106*, 641-646. doi:10.1073/pnas.0805165106.
40. Liebner, S., Corada, M., Bangsow, T., Babbage, J., Taddei, A., Czupalla, C.J., Reis, M., Felici, A., Wolburg, H., Fruttiger, M., et al. (2008). Wnt/beta-catenin signaling controls development of the blood-brain barrier. J Cell Biol *183*, 409-417. 10.1083/jcb.200806024.
41. Vanhollebeke, B., Stone, O.A., Bostaille, N., Cho, C., Zhou, Y., Maquet, E., Gauquier, A., Cabochette, P., Fukuhara, S., Mochizuki, N., et al. (2015). Tip cell-specific requirement for an atypical Gpr124- and Reck-dependent Wnt/β-catenin pathway during brain angiogenesis. eLife *4*, e06489. 10.7554/eLife.06489.
42. Hupe, M., Li, M.X., Kneitz, S., Davydova, D., Yokota, C., Kele, J., Hot, B., Stenman, J.M., and Gessler, M. (2017). Gene expression profiles of brain endothelial cells during embryonic development at bulk and single-cell levels. Science Signaling *10*, eaag2476. doi:10.1126/scisignal.aag2476.
43. Sabbagh, M.F., Heng, J.S., Luo, C., Castanon, R.G., Nery, J.R., Rattner, A., Goff, L.A., Ecker, J.R., and Nathans, J. (2018). Transcriptional and epigenomic landscapes of CNS and non-CNS vascular endothelial cells. eLife *7*, e36187. 10.7554/eLife.36187.
44. Reyahi, A., Nik, Ali M., Ghiami, M., Gritli-Linde, A., Pontén, F., Johansson, Bengt R., and Carlsson, P. (2015). Foxf2 Is Required for Brain Pericyte Differentiation and Development and

Maintenance of the Blood-Brain Barrier. Developmental Cell *34*, 19-32. https://doi.org/10.1016/j.devcel.2015.05.008.

45. Sadanandan, J., Thomas, S., Mathew, I.E., Huang, Z., Blackburn, S.L., Tandon, N., Lokhande, H., McCrea, P.D., Bresnick, E.H., Dash, P.K., et al. (2023). Establishing And Maintaining The Blood-Brain Barrier: Epigenetic And Signaling Determinants. eLife Sciences Publications, Ltd.

46. Praca, C., Rosa, S.C., Sevin, E., Cecchelli, R., Dehouck, M.P., and Ferreira, L.S. (2019). Derivation of Brain Capillary-like Endothelial Cells from Human Pluripotent Stem Cell-Derived Endothelial Progenitor Cells. Stem Cell Reports *13*, 599-611. 10.1016/j.stemcr.2019.08.002.

47. Engelhardt, B., and Liebner, S. (2014). Novel insights into the development and maintenance of the blood–brain barrier. Cell and Tissue Research *355*, 687-699. 10.1007/s00441-014-1811-2.

48. Praça, C., Rosa, S.C., Sevin, E., Cecchelli, R., Dehouck, M.P., and Ferreira, L.S. (2019). Derivation of Brain Capillary-like Endothelial Cells from Human Pluripotent Stem Cell-Derived Endothelial Progenitor Cells. Stem Cell Reports *13*, 599-611. 10.1016/j.stemcr.2019.08.002.

49. Mikami, Y., Grubb, B.R., Rogers, T.D., Dang, H., Asakura, T., Kota, P., Gilmore, R.C., Okuda, K., Morton, L.C., Sun, L., et al. (2023). Chronic airway epithelial hypoxia exacerbates injury in muco-obstructive lung disease through mucus hyperconcentration. Science Translational Medicine *15*, eabo7728. doi:10.1126/scitranslmed.abo7728.

50. Singh, N., Eickhoff, C., Garcia-Agundez, A., Bertone, P., Paudel, S.S., Tambe, D.T., Litzky, L.A., Cox-Flaherty, K., Klinger, J.R., Monaghan, S.F., et al. (2023). Transcriptional profiles of pulmonary artery endothelial cells in pulmonary hypertension. Sci Rep *13*, 22534. 10.1038/s41598-023-48077-6.

51. Uhl, K., Paithankar, S., Leshchiner, D., Jager, T.E., Abdelgied, M., Dixit, B., Marashdeh, R., Luo-Li, D., Tripp, K., Peraino, A.M., et al. (2023). Differential Transcriptomic Signatures of Small Airway Cell Cultures Derived from IPF and COVID-19-Induced Exacerbation of Interstitial Lung Disease. Cells *12*, 2501.

52. Zhao, Z., Nelson, A.R., Betsholtz, C., and Zlokovic, B.V. (2015). Establishment and Dysfunction of the Blood-Brain Barrier. Cell *163*, 1064-1078. 10.1016/j.cell.2015.10.067.

53. Miller, D.W., Batrakova, E.V., Waltner, T.O., Alakhov, V., and Kabanov, A.V. (1997). Interactions of pluronic block copolymers with brain microvessel endothelial cells: evidence of two potential pathways for drug absorption. Bioconjug Chem *8*, 649-657. 10.1021/bc970118d.

54. Revesz, T., Holton, J.L., Lashley, T., Plant, G., Frangione, B., Rostagno, A., and Ghiso, J. (2009). Genetics and molecular pathogenesis of sporadic and hereditary cerebral amyloid angiopathies. Acta Neuropathol *118*, 115-130. 10.1007/s00401-009-0501-8.

55. Santos, C.Y., Snyder, P.J., Wu, W.C., Zhang, M., Echeverria, A., and Alber, J. (2017). Pathophysiologic relationship between Alzheimer's disease, cerebrovascular disease, and cardiovascular risk: A review and synthesis. Alzheimers Dement (Amst) *7*, 69-87. 10.1016/j.dadm.2017.01.005.

56. Toledo, J.B., Arnold, S.E., Raible, K., Brettschneider, J., Xie, S.X., Grossman, M., Monsell, S.E., Kukull, W.A., and Trojanowski, J.Q. (2013). Contribution of cerebrovascular disease in autopsy confirmed neurodegenerative disease cases in the National Alzheimer's Coordinating Centre. Brain *136*, 2697-2706. 10.1093/brain/awt188.

57. Biffi, A., and Greenberg, S.M. (2011). Cerebral amyloid angiopathy: a systematic review. J Clin Neurol *7*, 1-9. 10.3988/jcn.2011.7.1.1.

58. Dimitrijevic, O.B., Stamatovic, S.M., Keep, R.F., and Andjelkovic, A.V. (2006). Effects of the chemokine CCL2 on blood-brain barrier permeability during ischemia-reperfusion injury. J Cereb Blood Flow Metab *26*, 797-810. 10.1038/sj.jcbfm.9600229.

59. Schellenberg, A.E., Buist, R., Del Bigio, M.R., Toft-Hansen, H., Khorooshi, R., Owens, T., and Peeling, J. (2012). Blood-brain barrier disruption in CCL2 transgenic mice during pertussis toxin-induced brain inflammation. Fluids Barriers CNS *9*, 10. 10.1186/2045-8118-9-10.

60. Guo, F., Xu, D., Lin, Y., Wang, G., Wang, F., Gao, Q., Wei, Q., and Lei, S. (2020). Chemokine CCL2 contributes to BBB disruption via the p38 MAPK signaling pathway following acute intracerebral hemorrhage. FASEB J *34*, 1872-1884. 10.1096/fj.201902203RR.
61. Cottarelli, A., Shahriar, S., Arac, A., Glendinning, M., Tuohy, M.C., Prochilo, G., Neal, J.B., Edinger, A.L., and Agalliu, D. (2023). Rab7a activation promotes degradation of select tight junction proteins at the blood-brain barrier after ischemic stroke. bioRxiv. 10.1101/2023.08.29.555373.
62. Shin, Y.J., Evitts, K.M., Jin, S., Howard, C., Sharp-Milgrom, M., Schwarze-Taufiq, T., Kinoshita, C., Young, J.E., and Zheng, Y. (2023). Amyloid beta peptides (Abeta) from Alzheimer's disease neuronal secretome induce endothelial activation in a human cerebral microvessel model. Neurobiol Dis *181*, 106125. 10.1016/j.nbd.2023.106125.
63. Kano, A., Wolfgang, M.J., Gao, Q., Jacoby, J., Chai, G.X., Hansen, W., Iwamoto, Y., Pober, J.S., Flavell, R.A., and Fu, X.Y. (2003). Endothelial cells require STAT3 for protection against endotoxin-induced inflammation. J Exp Med *198*, 1517-1525. 10.1084/jem.20030077.
64. Mehla, J., Singh, I., Diwan, D., Nelson, J.W., Lawrence, M., Lee, E., Bauer, A.Q., Holtzman, D.M., and Zipfel, G.J. (2021). STAT3 inhibitor mitigates cerebral amyloid angiopathy and parenchymal amyloid plaques while improving cognitive functions and brain networks. Acta Neuropathol Commun *9*, 193. 10.1186/s40478-021-01293-5.
65. Ehlers, H., Nicolas, A., Schavemaker, F., Heijmans, J.P.M., Bulst, M., Trietsch, S.J., and van den Broek, L.J. (2023). Vascular inflammation on a chip: A scalable platform for trans-endothelial electrical resistance and immune cell migration. Front Immunol *14*, 1118624. 10.3389/fimmu.2023.1118624.
66. Wevers, N.R., Kasi, D.G., Gray, T., Wilschut, K.J., Smith, B., van Vught, R., Shimizu, F., Sano, Y., Kanda, T., Marsh, G., et al. (2018). A perfused human blood-brain barrier on-a-chip for high-throughput assessment of barrier function and antibody transport. Fluids Barriers CNS *15*, 23. 10.1186/s12987-018-0108-3.
67. Lian, X., Bao, X., Al-Ahmad, A., Liu, J., Wu, Y., Dong, W., Dunn, K.K., Shusta, E.V., and Palecek, S.P. (2014). Efficient differentiation of human pluripotent stem cells to endothelial progenitors via small-molecule activation of WNT signaling. Stem Cell Reports *3*, 804-816. 10.1016/j.stemcr.2014.09.005.
68. Moir, R.D., Lathe, R., and Tanzi, R.E. (2018). The antimicrobial protection hypothesis of Alzheimer's disease. Alzheimers Dement *14*, 1602-1614. 10.1016/j.jalz.2018.06.3040.
69. Inoue, Y., Ando, Y., Misumi, Y., and Ueda, M. (2021). Current Management and Therapeutic Strategies for Cerebral Amyloid Angiopathy. Int J Mol Sci *22*. 10.3390/ijms22083869.
70. Yu, J., Vodyanik, M.A., Smuga-Otto, K., Antosiewicz-Bourget, J., Frane, J.L., Tian, S., Nie, J., Jonsdottir, G.A., Ruotti, V., Stewart, R., et al. (2007). Induced pluripotent stem cell lines derived from human somatic cells. Science *318*, 1917-1920. 10.1126/science.1151526.
71. Tchieu, J., Calder, E.L., Guttikonda, S.R., Gutzwiller, E.M., Aromolaran, K.A., Steinbeck, J.A., Goldstein, P.A., and Studer, L. (2019). NFIA is a gliogenic switch enabling rapid derivation of functional human astrocytes from pluripotent stem cells. Nat Biotechnol *37*, 267-275. 10.1038/s41587-019-0035-0.
72. Maherali, N., Ahfeldt, T., Rigamonti, A., Utikal, J., Cowan, C., and Hochedlinger, K. (2008). A high-efficiency system for the generation and study of human induced pluripotent stem cells. Cell Stem Cell *3*, 340-345. 10.1016/j.stem.2008.08.003.
73. Reya, T., Duncan, A.W., Ailles, L., Domen, J., Scherer, D.C., Willert, K., Hintz, L., Nusse, R., and Weissman, I.L. (2003). A role for Wnt signalling in self-renewal of haematopoietic stem cells. Nature *423*, 409-414. 10.1038/nature01593.

74. Song, S., Ashok, A., Williams, D., Kaufman, M., Duff, K., and Sproul, A. (2021). Efficient Derivation of Excitatory and Inhibitory Neurons from Human Pluripotent Stem Cells Stably Expressing Direct Reprogramming Factors. Curr Protoc *1*, e141. 10.1002/cpz1.141.
75. Faal, T., Phan, D.T.T., Davtyan, H., Scarfone, V.M., Varady, E., Blurton-Jones, M., Hughes, C.C.W., and Inlay, M.A. (2019). Induction of Mesoderm and Neural Crest-Derived Pericytes from Human Pluripotent Stem Cells to Study Blood-Brain Barrier Interactions. Stem Cell Reports *12*, 451-460. https://doi.org/10.1016/j.stemcr.2019.01.005.
76. Tcw, J., Wang, M., Pimenova, A.A., Bowles, K.R., Hartley, B.J., Lacin, E., Machlovi, S.I., Abdelaal, R., Karch, C.M., Phatnani, H., et al. (2017). An Efficient Platform for Astrocyte Differentiation from Human Induced Pluripotent Stem Cells. Stem Cell Reports *9*, 600-614. https://doi.org/10.1016/j.stemcr.2017.06.018.
77. Suarez-Arnedo, A., Torres Figueroa, F., Clavijo, C., Arbeláez, P., Cruz, J.C., and Muñoz-Camargo, C. (2020). An image J plugin for the high throughput image analysis of in vitro scratch wound healing assays. PLoS One *15*, e0232565. 10.1371/journal.pone.0232565.
78. Stine, W.B., Jr., Dahlgren, K.N., Krafft, G.A., and LaDu, M.J. (2003). In vitro characterization of conditions for amyloid-beta peptide oligomerization and fibrillogenesis. J Biol Chem *278*, 11612-11622. 10.1074/jbc.M210207200.
79. Kim, Y.A., Siddiqui, T., Blaze, J., Cosacak, M.I., Winters, T., Kumar, A., Tein, E., Sproul, A.A., Teich, A.F., Bartolini, F., et al. (2023). RNA methyltransferase NSun2 deficiency promotes neurodegeneration through epitranscriptomic regulation of tau phosphorylation. Acta Neuropathol *145*, 29-48. 10.1007/s00401-022-02511-7.

FIGURE LEGENDS

Figure 1: rBMECs transdifferentiated from bpECs show markers of brain endothelial cells and have angiogenic properties. A) Cartoon schematic showing differentiation of iPSCs to bpECs and rBMECs. **B)** Representative flow cytometry plots showing sort A (bpECs) at day 10 of differentiation and sort B (rBMECs) at day 14 post-transduction of bpECs; cell populations circled are showing $CD31^+$/VE-$cadherin^+$ endothelial cell populations. **C)** Comparison of $CD31^+$/VE-$cadherin^+$ endothelial cells for uninfected bpECs and rBMECs, N = 5; bpECs were used in each sort as uninfected controls cultured in parallel with rBMECs transdifferentiation period of 14-days post-transduction. Statistical comparisons were made between bpECs and rBMECs groups using unpaired t-test, ** <0.01. N=5. **D)** Representative immunofluorescence images of endothelial cell markers CD31 (green) and VE-cadherin (red) staining; DAPI (blue) in merge panel; each image shows 150 μm area, scale bar = 25 μm. **E)** Representative IF for tight junction marker Occludin; scale bar = 25 μm. **F)** Representative immunofluorescence images of TJ markers claudin-5 (green) and ZO-1 (red) staining; scale bar = 25 μm. **G)** Representative western blot images of Claudin-5 (18 kD), Occludin (52 kD) and loading control GAPDH (37 kD), N=3. **H)** Densitometry quantification of western blots for Claudin-5 and Occludin; GAPDH is loading control; 3 independent differentiations, N=9; unpaired t-test, **<0.1, ***<0.001. **I)** Proliferative index quantification from the cell migration assay, 3 independent experiments, N=8-9; one-way ANOVA, ns, ****<0.0001. **J)** Summary of wound size in normalized area pixels from a wound scratch and measurement of wound size every 6 hrs; unpaired t-test at each time point, with N=9 across three independent experiments, *<0.05, ** <0.1, ***<0.001, ****<0.0001. **K)** Quantification of angiogenic potential in the untreated and angiogenic cocktail treated conditions from panel J, 3 independent experiments, N=9; statistical comparisons were made using one-way ANOVA, ns, ***<0.001.

Figure 2: Transcriptomic analysis shows rBMECs acquire a BBB-molecular profile compared to primary HBMECs. A) Principal component analysis (PCA) plot approximating relative relationships of 155 distinct cell samples across 24 library preparations from previously published and newly generated bulk RNA-sequencing data. B) Principal component analysis plot approximating the relative relationship of 58 distinct cell samples including other differentiation protocols as well as primary endothelial cells from published data sets, across 10 library preparations from previously published and newly generated bulk RNA-sequencing data. C-F) Heatmaps of showing the comparison of BBB specific (TJ proteins, Transporters, Bulk and Receptor-Mediated Transcytosis, Extracellular

matrix, and CNS EC genes) genes between rBMEC and HBMECs. Genes are highlighted in red are upregulated in rBMECs, genes are highlighted blue are showing upregulation in HBMECs ($p<0.05$ and Log2FC <0.25). G) Volcano plot highlighting genes that are up-regulated and down-regulated in rBMECs compared to hBMECs. BBB-specific genes are enlisted, all genes are statistically significant ($p<0.05$, logFC < or > 0.25). H) GO analysis of differentially expressed genes in rBMECs compared to HBMECs showing significantly up-regulated pathways.

Figure 3: rBMECs show improved barrier tightness, functional efflux transporter activity, low transcytosis and reactivity to disease-relevant proinflammatory stimuli. A) Representative ECIS TEER recording of HBMECs, bpECs and rBMECs, red boxed area shows last 100 hours used for AUC calculations in panel B. **B)** Quantification of AUC for last 100 hours of TEER measurement; each dot on the graph represents combined AUC value from 6-8 wells as one independent biological replicate from 3-4 independent experiments; mean±SD, N=6-8, one-way ANOVA, ns, **<0.01. **C-D)** Representative histograms and quantification of BSA-AF594 uptake by flow cytometry; mean±SD, one-way ANOVA, N=9, ns, ****<0.0001. **E-G)** Representative histograms, PGP efflux, and MFI quantification of Rhodamine 123 uptake assay; PSC-833, p-glycoprotein inhibitor; mean±SD from 3 independent experiment, N=9; one-way ANOVA, ns, **<0.01. **I)** Representative TEER of rBMECs with F12 vehicle control and 1 uM oAβ42 for 72 hours (red arrow shows start of treatment) in panel **J)** AUC quantification of TEER for treatment period of oAβ42; mean ± SD from 3 independent experiments, where each dot is combined value of 6-8 wells; N=9-10, unpaired t-test, ns. **K)** RT-qPCR quantification of surface adhesion molecules *(ICAM-1*, *VCAM-1* and *E-SELECTIN*), chemoattractant (*CCL2*) and proinflammatory cytokines (*IL1β*, *IL6* and *TNFα*) transcription are shown for rBMECs treated with 500nM oAβ42 for 6 hours, mean±SD for 3 independent experiments, N=8-9; unpaired t-test, **<0.01, ***<0.001, ****<0.0001 **L)** Flow cytometry quantification of VCAM-1 and ICAM-1 surface expression on rBMECs treated with 500nM oAβ42 for 6 hours; mean±SD for 2 independent experiments, N=6; unpaired t-test, **<0.01, ****<0.0001 **M-N)** Representative western blots and respective quantifications of VCAM-1 with loading control GAPDH for rBMECs when treated with 500nM oAβ42 for 6 hours. Quantification presented as mean ± SD from 2 independent experiments, N=6; unpaired t-test, ***<0.001.

Figure 4: rBMECs tubules have improved barrier properties when co-cultured with iPSC-derived astrocytes and pericytes in a 3D microfluidic NVU system. A) Schematic showing the process of generating the 3D NVU system in the MIMETAS microfluidic system. **B)** Brightfield images showing

HBMEC and rBMEC only tubules, as well as their co-cultures with primary astrocytes (AC) and primary pericytes (PC) or iPSC-derived astrocytes (iACs) and pericytes (iPCs), respectively. **C)** Representative immunofluorescence staining images for rBMECs showing endothelial marker CD31 and VE-cadherin (top panel) and junctional expression of TJ markers ZO-1 and Claudin-5 (bottom panel) in tubules formed inside 3D microfluidic channels; scale bar = 50 µm **D)** 3D view of representative immunofluorescence staining for MIMETAS microfluidic culture showing all three channels with PDGFRβ^+ pericytes and S100β^+ astrocytes in brain channel and rBMEC tubule in the blood channel. **E)** Close up view of representative immunofluorescence staining showing TJ marker ZO-1 for rBMECs, S100β for astrocytes, and PDGFRβ for pericytes in the blood channel; cross sectional view shows tubule with open lumen. **F)** Representative image showing differential diffusion of fluorescent tracer from leaky and tight barriers in 3D microfluidic culture. **G-H)** Permeability measurement of primary HBMEC tubules, HBMEC tubules with ACs and PCs, rBMEC tubules, and rBMEC tubules with iACs and iPCs in the middle ECM channel using large 70 kDa dextran and small ~900Da Biocytin tracer over a course of 45 minutes. N=36-41 NVU chips. Data was analyzed using two-way ANOVA and presented as mean±SD for 3 independent experiments, ns, **<0.01, ****<0.0001. **I)** 3D TEER measurement comparing primary HBMEC tubules, HBMEC tubules with ACs and PCs, rBMEC tubules, and rBMEC tubules with iACs and iPCs; each point represents one individual NVU chip. N = 30-48. Data is presented as mean±SD, and statistical comparisons were made between each group using one-way ANOVA, ****<0.0001, *<0.05.

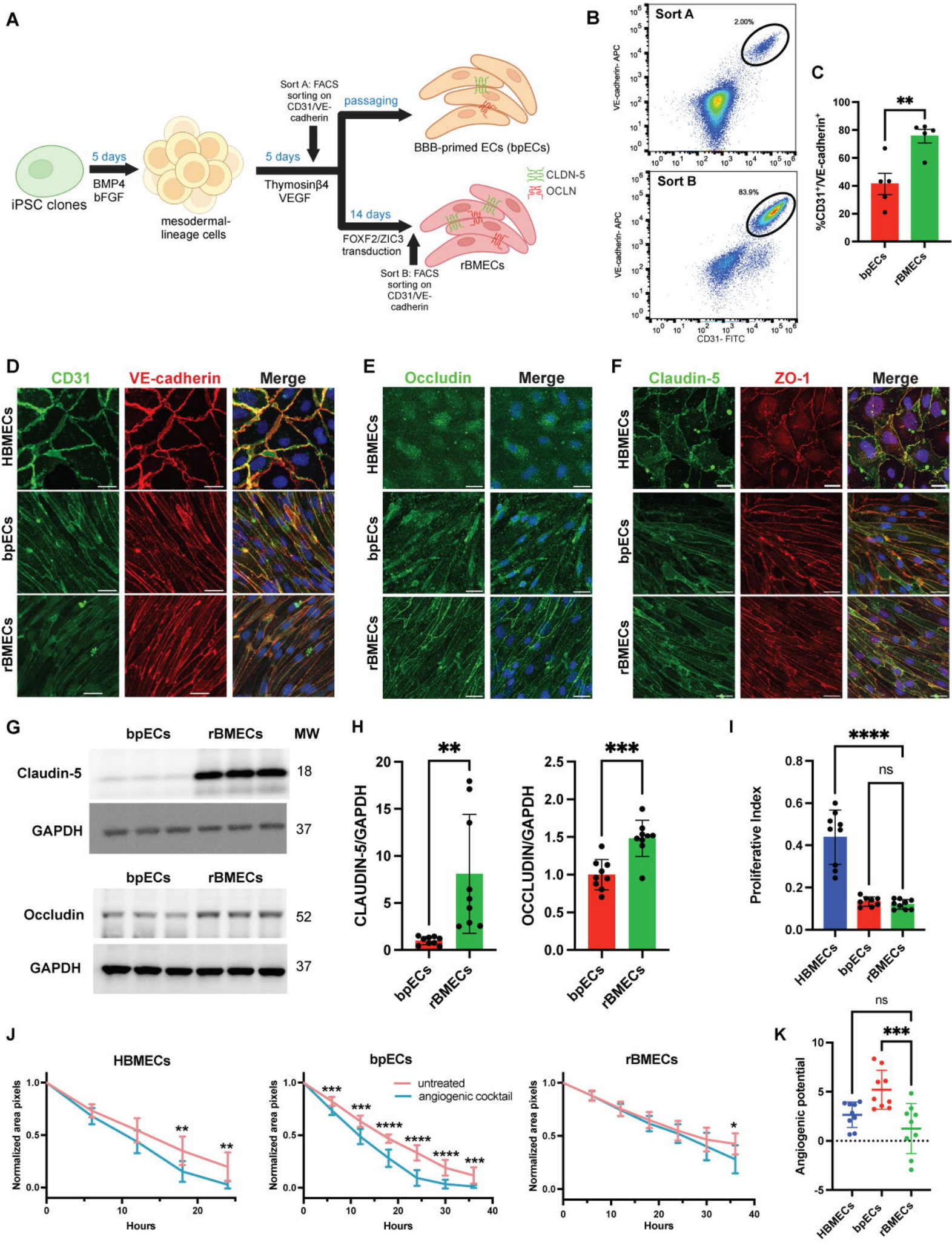
A
iPSC clones
5 days
BMP4
bFGF
mesodermal-lineage cells
Sort A: FACS sorting on CD31/VE-cadherin
5 days
Thymosinβ4
VEGF
passaging
BBB-primed ECs (bpECs)
CLDN-5
OCLN
14 days
FOXF2/ZIC3 transduction
rBMECs
Sort B: FACS sorting on CD31/VE-cadherin
B
Sort A
2.00%
Sort B
83.9%
VE-cadherin- APC
CD31- FITC
C
%CD31+/VE-cadherin+
bpECs
rBMECs
D
CD31
VE-cadherin
Merge
HBMECs
bpECs
rBMECs
E
Occludin
Merge
F
Claudin-5
ZO-1
Merge
G
bpECs
rBMECs
MW
Claudin-5
18
GAPDH
37
Occludin
52
H
CLAUDIN-5/GAPDH
OCCLUDIN/GAPDH
I
Proliferative Index
ns
J
HBMECs
bpECs
rBMECs
Normalized area pixels
Hours
untreated
angiogenic cocktail
K
Angiogenic potential

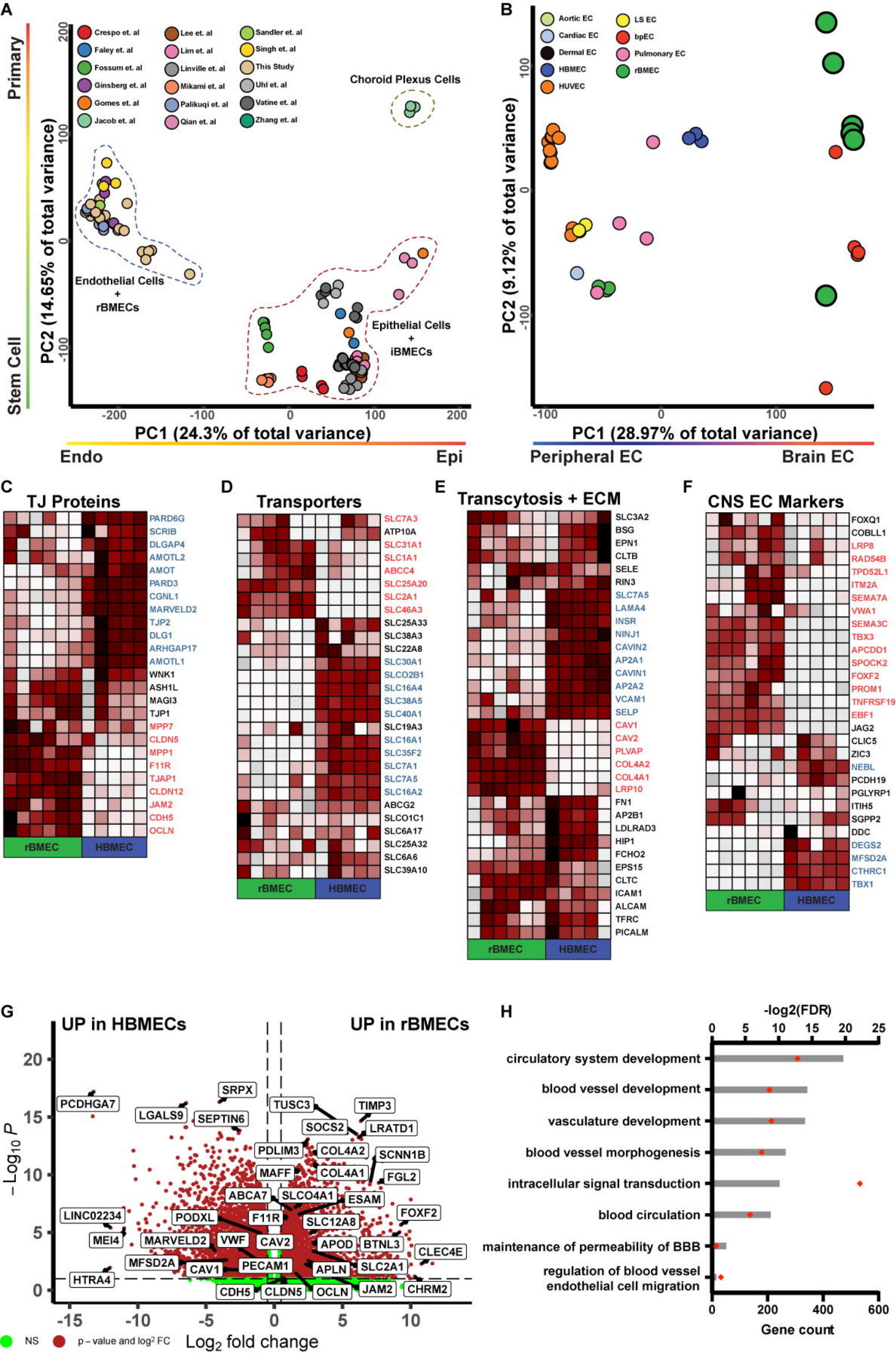
A
Primary
Stem Cell
Crespo et. al
Faley et. al
Fossum et. al
Ginsberg et. al
Gomes et. al
Jacob et. al
Lee et. al
Lim et. al
Linville et. al
Mikami et. al
Palikuqi et. al
Qian et. al
Sandler et. al
Singh et. al
This Study
Uhl et. al
Vatine et. al
Zhang et. al
Choroid Plexus Cells
Endothelial Cells
+
rBMECs
Epithelial Cells
+
iBMECs
PC2 (14.65% of total variance)
PC1 (24.3% of total variance)
Endo
Epi
B
Aortic EC
Cardiac EC
Dermal EC
HBMEC
HUVEC
LS EC
bpEC
Pulmonary EC
rBMEC
PC2 (9.12% of total variance)
PC1 (28.97% of total variance)
Peripheral EC
Brain EC
C
TJ Proteins
PARD6G
SCRIB
DLGAP4
AMOTL2
AMOT
PARD3
CGNL1
MARVELD2
TJP2
DLG1
ARHGAP17
AMOTL1
WNK1
ASH1L
MAGI3
TJP1
MPP7
CLDN5
MPP1
F11R
TJAP1
CLDN12
JAM2
CDH5
OCLN
rBMEC
HBMEC
D
Transporters
SLC7A3
ATP10A
SLC31A1
SLC1A1
ABCC4
SLC25A20
SLC2A1
SLC46A3
SLC25A33
SLC38A3
SLC22A8
SLC30A1
SLCO2B1
SLC16A4
SLC38A5
SLC40A1
SLC19A3
SLC16A1
SLC35F2
SLC7A1
SLC7A5
SLC16A2
ABCG2
SLCO1C1
SLC6A17
SLC25A32
SLC6A6
SLC39A10
rBMEC
HBMEC
E
Transcytosis + ECM
SLC3A2
BSG
EPN1
CLTB
SELE
RIN3
SLC7A5
LAMA4
INSR
NINJ1
CAVIN2
AP2A1
CAVIN1
AP2A2
VCAM1
SELP
CAV1
CAV2
PLVAP
COL4A2
COL4A1
LRP10
FN1
AP2B1
LDLRAD3
HIP1
FCHO2
EPS15
CLTC
ICAM1
ALCAM
TFRC
PICALM
rBMEC
HBMEC
F
CNS EC Markers
FOXQ1
COBLL1
LRP8
RAD54B
TPD52L1
ITM2A
SEMA7A
VWA1
SEMA3C
TBX3
APCDD1
SPOCK2
FOXF2
PROM1
TNFRSF19
EBF1
JAG2
CLIC5
ZIC3
NEBL
PCDH19
PGLYRP1
ITIH5
SGPP2
DDC
DEGS2
MFSD2A
CTHRC1
TBX1
rBMEC
HBMEC
G
UP in HBMECs
UP in rBMECs
PCDHGA7
LGALS9
SEPTIN6
SRPX
TUSC3
TIMP3
SOCS2
LRATD1
PDLIM3
COL4A2
SCNN1B
MAFF
COL4A1
FGL2
ABCA7
SLCO4A1
ESAM
LINC02234
PODXL
F11R
SLC12A8
FOXF2
MEI4
MARVELD2
VWF
CAV2
APOD
BTNL3
CLEC4E
MFSD2A
CAV1
PECAM1
APLN
SLC2A1
HTRA4
CDH5
CLDN5
OCLN
JAM2
CHRM2
$-\text{Log}_{10}\,P$
Log_2 fold change
NS
p – value and log2 FC
H
-log2(FDR)
circulatory system development
blood vessel development
vasculature development
blood vessel morphogenesis
intracellular signal transduction
blood circulation
maintenance of permeability of BBB
regulation of blood vessel endothelial cell migration
Gene count

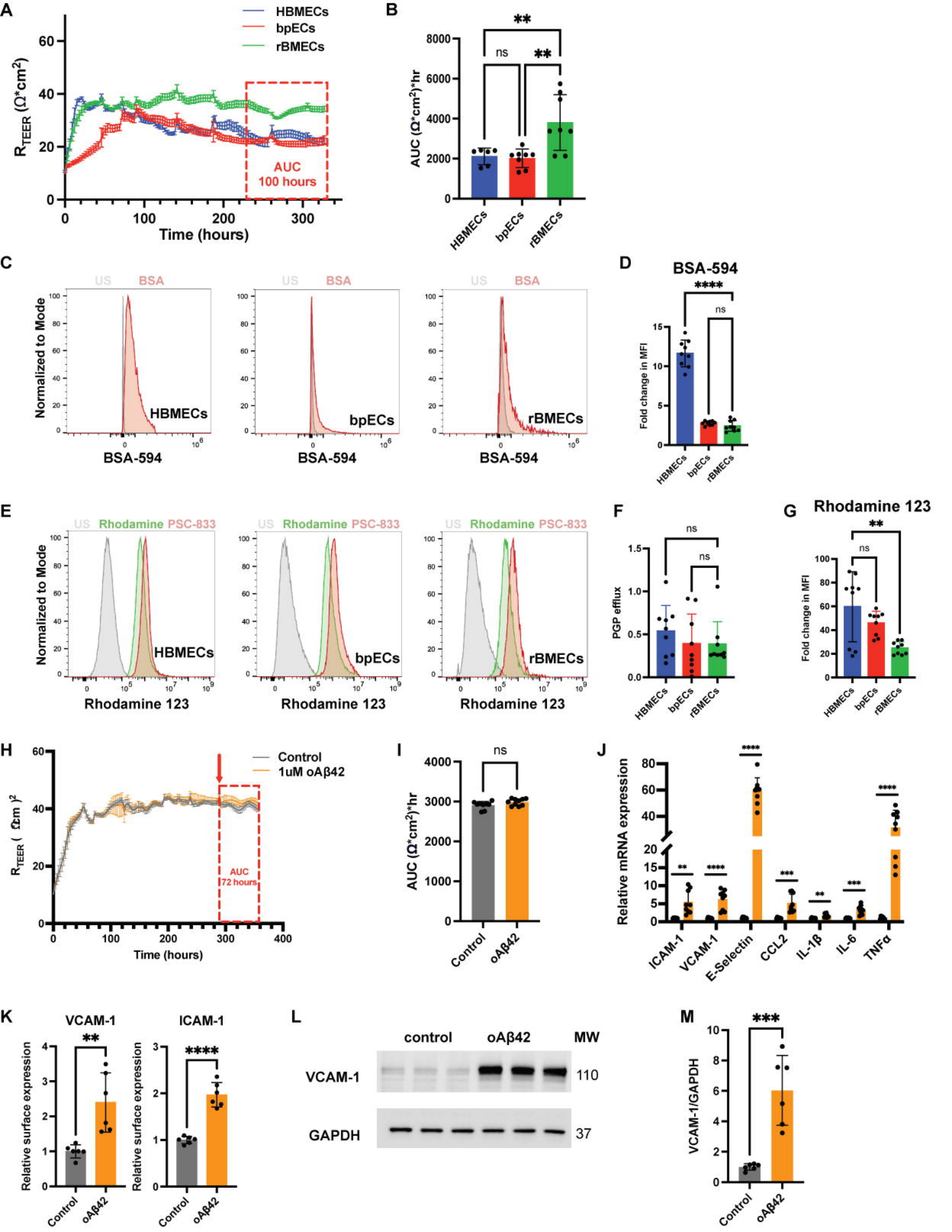
A
HBMECs
bpECs
rBMECs
R_{TEER} (Ω*cm^2)
AUC
100 hours
Time (hours)
B
AUC (Ω*cm^2)*hr
ns
**
HBMECs
bpECs
rBMECs
C
US
BSA
Normalized to Mode
HBMECs
bpECs
rBMECs
BSA-594
D
BSA-594
****
ns
Fold change in MFI
E
Rhodamine PSC-833
Rhodamine 123
F
PGP efflux
G
Rhodamine 123
H
Control
1uM oAβ42
AUC
72 hours
I
J
Relative mRNA expression
ICAM-1
VCAM-1
E-Selectin
CCL2
IL-1β
IL-6
TNFα
K
VCAM-1
ICAM-1
Relative surface expression
Control
oAβ42
L
control
oAβ42
MW
110
37
M
VCAM-1/GAPDH

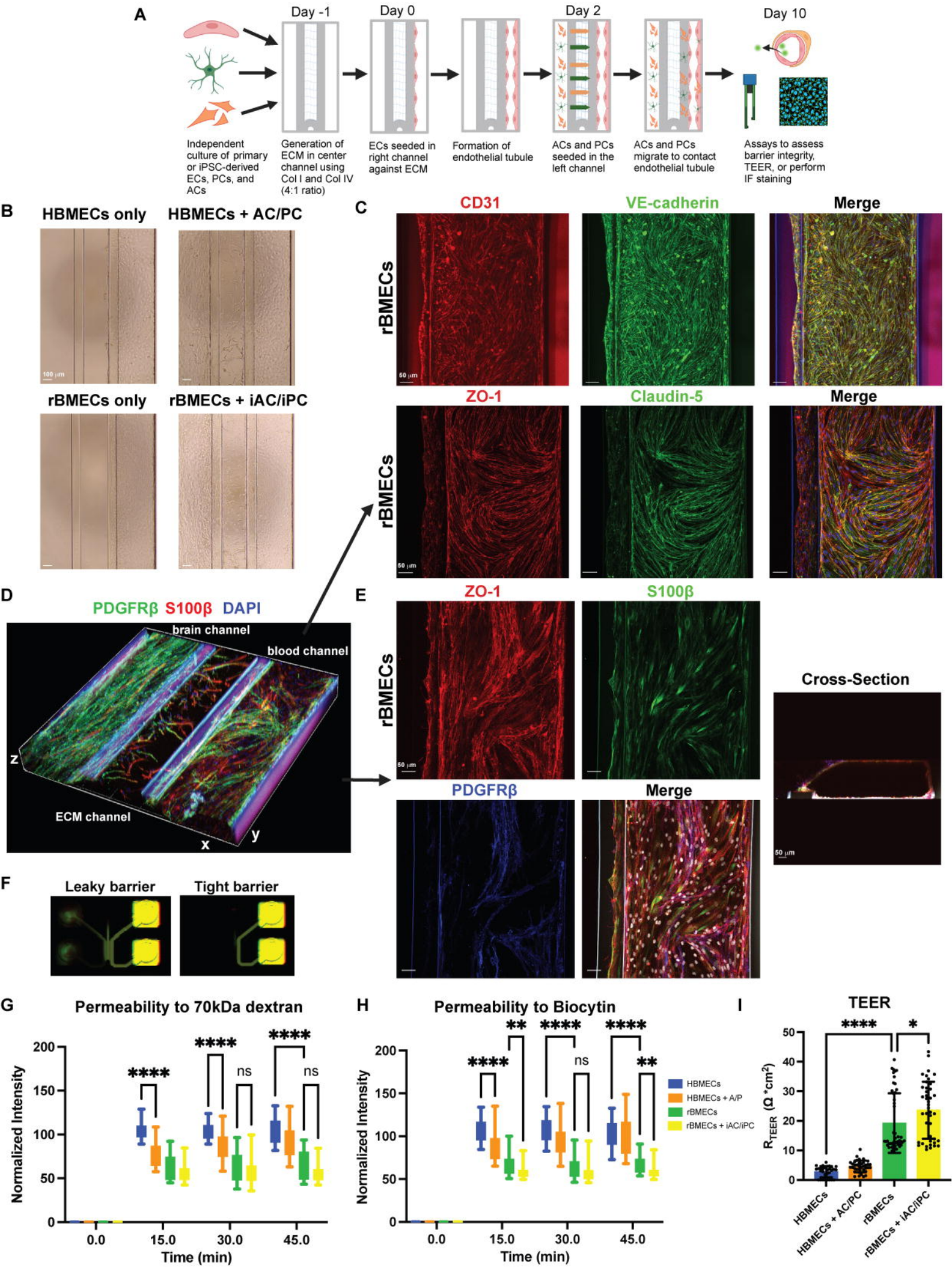
A
Day -1
Day 0
Day 2
Day 10
Independent culture of primary or iPSC-derived ECs, PCs, and ACs
Generation of ECM in center channel using Col I and Col IV (4:1 ratio)
ECs seeded in right channel against ECM
Formation of endothelial tubule
ACs and PCs seeded in the left channel
ACs and PCs migrate to contact endothelial tubule
Assays to assess barrier integrity, TEER, or perform IF staining
B
HBMECs only
HBMECs + AC/PC
rBMECs only
rBMECs + iAC/iPC
C
CD31
VE-cadherin
Merge
rBMECs
ZO-1
Claudin-5
Merge
rBMECs
D
PDGFRβ S100β DAPI
brain channel
blood channel
ECM channel
z
x
y
E
ZO-1
S100β
rBMECs
PDGFRβ
Merge
Cross-Section
F
Leaky barrier
Tight barrier
G
Permeability to 70kDa dextran
Normalized Intensity
Time (min)
0.0
15.0
30.0
45.0
****
ns
H
Permeability to Biocytin
Normalized Intensity
Time (min)
HBMECs
HBMECs + A/P
rBMECs
rBMECs + iAC/iPC
I
TEER
R_{TEER} (Ω *cm^2)
HBMECs
HBMECs + AC/PC
rBMECs
rBMECs + iAC/iPC